**Department of Physics and Astronomy**
**Heidelberg University**

Bachelor Thesis in Physics
submitted by

**Carlotta Rosenthal**

born in Hamburg (Germany)

**2022**

# Estimated number of $\chi_c$-states in pp collisions at $\sqrt{s} = 13$ TeV with ALICE in LHC Run 3

This Bachelor Thesis has been carried out by Carlotta Rosenthal at the
Physikalisches Institut in Heidelberg
under the supervision of
Priv. Doz. Dr. Yvonne Pachmayer

# Abstract

This thesis provides estimates for the number of $\chi_{c1}$ and $\chi_{c2}$ states at the centre-of-mass energy $\sqrt{s}$ = 13 TeV in pp collisions for ALICE in LHC Run 3 for different integrated luminosities. For this, the $\chi_c$ mesons are studied in the radiative $J/\psi$ decay channel $\chi_c \rightarrow \gamma J/\psi$, using the $J/\psi$ reconstructed in the $e^+e^-$ and the radiative decay channel. The Monte Carlo simulation of the $\chi_c$ mesons includes the realistic detector acceptance, the lepton, $J/\psi$ and photon reconstruction efficiencies and photon conversion probability in the detector material based on Run 2 measurements.



# Zusammenfassung

Diese Arbeit liefert Abschätzungen für die Anzahl der $\chi_{c1}$- und $\chi_{c2}$-Zustände bei einer Schwerpunktsenergie von $\sqrt{s}$ = 13 TeV in pp-Kollisionen für ALICE in LHC Run 3 für verschiedene integrierte Luminositäten. Dazu werden die $\chi_c$-Mesonen im radiativen $J/\psi$-Zerfallskanal $\chi_c \rightarrow \gamma J/\psi$ untersucht, wobei die im $e^+e^-$- und dem radiativen Zerfallskanal rekonstruierten $J/\psi$ verwendet werden. Die Monte-Carlo-Simulation der $\chi_c$-Mesonen beinhaltet eine realistische Detektorakzeptanz und die Rekonstruktionseffizienzen von Leptonen, $J/\psi$ und Photonen sowie die Wahrscheinlichkeit der Photonenkonversion im Detektor auf der Grundlage von Run-2-Messungen.

# Contents

# Chapter 1

# Introduction and Theoretical Background

## 1.1 Motivation

Charmonium ($c\overline{c}$) production in hadronic collisions is of considerable interest for understanding hadronisation (the process of the formation of hadrons out of quarks and gluons) in quantum chromodynamics (QCD). Most experimental observations of charmonium production consist of $J/\psi$ measurements. A significant contribution of $J/\psi$ production is indirect, resulting from the decay of higher mass states, in particular, the radiative decay of the $\chi_c$ states. Compared to proton-proton (pp) collisions, charmonium production is suppressed by the quark gluon plasma (QGP) in lead-lead (PbPb) collisions at medium and high momenta. However, there is an increased production at small momenta at medium rapidity. Measurements in pp collision without QGP act as a reference for measurements with QGP as well as improve theoretical pertubative QCD calculations.

This study calculates the estimated number of $\chi_c$ states in pp collisions at $\sqrt{s} = 13$ TeV for various running scenarios in LHC Run 3 with ALICE.
The simulated $\chi_c$ mesons are reconstructed through their radiative decay $\chi_c \rightarrow J/\psi + \gamma$, using the ALICE $J/\psi$ reconstructed in the $e^+e^-$. Not all three $\chi_c$ states are considered in the estimates, since the $\chi_{c0} \rightarrow J/\psi + \gamma$ branching fraction is $\sim 30$ times smaller than that of the $\chi_{c1}$ and $\chi_{c2}$ and its yield is therefore not significant at the expected integrated lumiosities.
This thesis aims to estimate the number of $\chi_c$ states and their $p_T$-distributions in a $p_T$-range down to 0 GeV/$c$ and analyse the effect of different single lepton selection criteria.

## 1.2 Standard Model

The Standard Model (SM) is the most successful theory of particle physics to date. It describes the smallest experimentally observed particles of matter (classifying all elementary particles) and their interactions. The SM describes the set of three of the four fundamental forces, namely the electromagnetic, weak and strong interactions. It omits gravity, which is one of the reasons why the SM is not a complete theory.

In the SM, the elementary particles are divided into two groups, namely the fermions and the bosons.
The gauge bosons with spin 1 act as mediators of interactions between fermions. The SM of particle physics has a total of twelve gauge bosons (on the right of Fig. 1.1): the photon, three weak bosons and eight gluons. Photons mediate the electromagnetic interaction, $W^{\pm}$ and $Z$ bosons the weak interaction and gluons the strong interaction.
The final element of the SM is the Higgs boson, a spin 0 scalar particle [1].

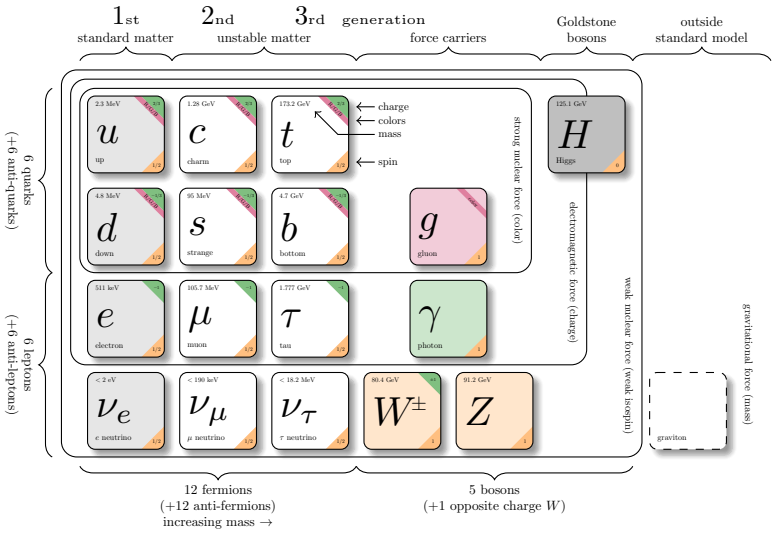


Figure 1.1: The elementary particles, force carrying gauge bosons and interactions of the Standard Model of particle physics [2]

The twelve fermions (on the left of Fig. 1.1) are fundamental constituents of matter with spin 1/2. Their anti-particles (not depicted in Fig. 1.1) have the same mass and spin but opposite charge. The fermions are ranked in three generations, going from left to right. The fermions of the first generation on the left of Fig. 1.1 are the basic building blocks of ordinary matter: protons and neutrons consist of up and down quarks, electrons surround atomic nuclei and electron neutrinos are created in $\beta^+$ decays.

The fermions can be further distinguished between quarks and leptons.
There are six types of quarks, known as flavours: up (u), down (d), strange (s), charm (c), bottom (b) and top (t). Quarks obey all three of the strong, weak and electromagnetic interactions. The quarks from higher generations possess larger masses, allowing them to decay to lighter quarks. Under standard conditions, owing to a phenomenon known as colour confinement (discussed in more detail in Section 1.3), quarks can be found only in bound states known as hadrons. There are two types of hadrons: mesons consist of a quark and an antiquark, baryons contain either three quarks or three antiquarks.
While quarks are confined to bound states, leptons are free in existence. The two main classes of leptons are charged leptons and their respective neutral leptons (neutrinos). The charged leptons electron ($e^-$), muon ($\mu^-$) and tau ($\tau^-$) with corresponding anti-particles ($e^+$, $\mu^+$, $\tau^+$) interact electromagnetically and weakly. Neutrinos ($\nu$) only interact weakly since they are not electromagnetically charged and are therefore difficult to detect. Their masses are too small to have been determined, upper limits on the possible neutrino masses of at least nine orders of magnitude lighter than the other fermions have been determined [1].

## 1.3 Quantum Chromodynamics and Hadronisation

Quantum Chromodynamics (QCD) is the theory of the SM describing the strong interactions. This section only gives a very brief insight, the key point to be made is that quarks cannot be observed as free particles under standard conditions.

Whilst the interaction in quantum electrodynamics (QED) is mediated by a massless photon, the interaction in QCD is mediated by eight massless gluons. In QED, particles can have one type of charge (antiparticles carry the opposite charge), in QCD there are three types of "colour" charge (again, antiparticles carry the opposite charges). Only particles with non-zero colour charges couple to gluons, the mediators of strong interaction, which is why leptons don't experience the strong force.
The concept of "colour confinement" implies that only colour singlet states, i.e. colourless combinations, can exist as free particles. Consequently, quarks are always confined to bound colourless states and only objects with zero colour charge can propagate as free particles. The precise process of the formation of colourless hadrons from quarks and antiquarks (hadronisation) is poorly understood. Most of the phenomenological models providing reasonable descriptions of experimental data are motivated by QCD.

Another consequence of QCD is the idea of asymptotic freedom. The so-called coupling constant $\alpha_S$ of QCD is large at low energy scales and small at high energy scales. This means that the strength of the interaction between quarks is strong at large separations and weakens as the quarks get closer to one another [1]. At high energies, QCD can be explained through perturbative theories, i.e. only the lowest-order term is significant. Low energy processes however cannot be explained by perturbation theories. Here, first-principle calculations such as the hadronisation process are not possible. Alternative theories such as lattice QCD have been developed.

## 1.4 Quark-Gluon Plasma

The idea of asymptotic freedom has a great consequence: At high enough temperatures and/or densities, the coupling constant approaches zero and the strongly interacting quarks and gluons become free and transform themselves into a state of matter in which they are no longer confined. This state is called 'quark–gluon plasma' (QGP).
The critical temperature between the confined hadronic phase and the deconfined plasma phase is estimated to be around $T_c = (156.5 \pm 1.5)$ MeV [3]. Such temperatures only ever existed in the electroweak phase transition that started around 10 picoseconds after the Big Bang and lasted for 10 microseconds. This is thought to have taken the form of QGP [4].
To create QGP, extremely high energy densities and temperatures as well as a large number of particles, ideally tens of thousands, are needed. Collisions of protons produce too few particles to fulfil these conditions. In ultra-relativistic heavy-ion collisions, however, such extreme conditions can be achieved for a short amount of time and a QGP can be created. The QGP then expands and cools, resulting in a transition back to confined matter (hadronisation). Due to much smaller energies in nuclear collisions in the laboratory than in the Big Bang, this happens at a time-scale of $\sim 10^{-22}$s [4]. Nonetheless, lead–lead collisions at the LHC studied with the specially designed ALICE detector (see Chapter 2) make it possible to quantify the QGP's physical properties as well as the processes of hadronisation.

One of the phenomena considered to be a signature of QGP production in collision at the LHC by ALICE is the suppression of the $J/\psi$ production due to the created medium. Figure 1.2 shows that large energies (at the LHC) increase the number of $c\bar{c}$ pairs by around a factor of 200 compared to lower energies (at the RHIC), making charmonium formation slightly more likely at the phase boundary. This so-called (re)generation is expected to have the most significant effect on the $J/\psi$ production at low $p_T$ at midrapidity due to a larger charm quark density. At large $p_T$, the $J/\psi$ production is suppressed due to colour screening and/or energy loss of charm quarks in the deconfined medium [4].

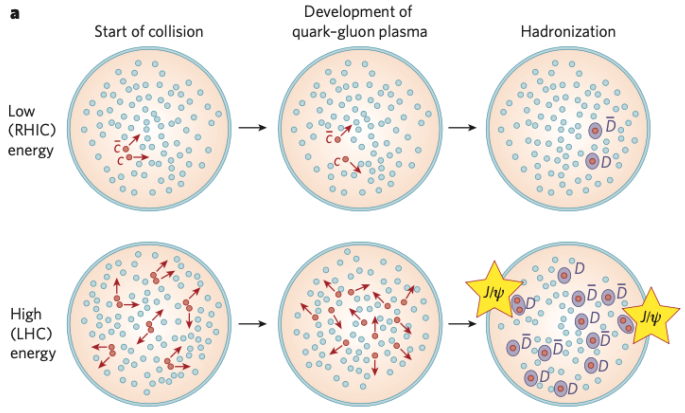


Figure 1.2: $J/\psi$ (re)generation at the LHC: At low energies, the QGP screens interaction between the only pair of $c\bar{c}$ produced; at hadronization, other two quarks (u, d, s) can pair with the $c$ or $\bar{c}$ to from D mesons. At high energies, many more $c\bar{c}$ pairs are produced; at hadronization, $c\bar{c}$ quarks from different original pairs can combine to form a charmonium $J/\psi$ particle [4]

## 1.5 The $J/\psi$ meson

The production of the $J/\psi$ meson is a well-studied subject of many theoretical calculations and experiments, [5, 6] are used in this thesis. It has a width of $\Gamma = (92.6 \pm 1.7)$ keV/$c^2$ and a mass of $m = (3096.900 \pm 0.006)$ MeV/$c^2$ [7].
The $J/\psi$ is an unstable particle and decays shortly after its production. The branching ratios of the most important decay channels are listed in Fig. 1.3:

| **$J/\psi(1S)$ DECAY MODES** | | Fraction ($\Gamma_i/\Gamma$) | Scale factor/ Confidence level | $p$ (MeV/$c$) |
|---|---|---|---|---|
| hadrons | | ( 87.7 ± 0.5 ) % | | – |
| virtual $\gamma \rightarrow$ hadrons | | ( 13.50 ± 0.30 ) % | | – |
| $ggg$ | | ( 64.1 ± 1.0 ) % | | – |
| $\gamma gg$ | | ( 8.8 ± 1.1 ) % | | – |
| $e^+e^-$ | | ( 5.971 ± 0.032) % | | 1548 |
| $e^+e^-\gamma$ | [a] | ( 8.8 ± 1.4 ) $\times 10^{-3}$ | | 1548 |
| $\mu^+\mu^-$ | | ( 5.961 ± 0.033) % | | 1545 |

Figure 1.3: The decay channels and branching ratios of the most important $J/\psi$ decay modes [7]

$J/\psi$ can be produced through different decays in hadronic collisions. In so-called prompt production, the $J/\psi$ is produced either through direct production of $J/\psi$ mesons from $c\bar{c}$ pairs produced during hard scattering or indirect production from the decay of higher mass states. In non-prompt production, the $J/\psi$ mesons come from decays of hadrons containing b quarks. Non-prompt production makes up approximately 10% of

the $J/\psi$ production at low $p_T$ up to approximately 3 GeV/$c$ and increases with increasing momentum.

## 1.6 The $\chi_c$ mesons

As mentioned above, a significant contribution of $J/\psi$ production is indirect. In particular, the radiative decay of the $\chi_c$ states accounts for a significant fraction of the $J/\psi$ production seen in hadronic collisions.
The level scheme in Fig. 1.4 shows the experimentally established states of charmonia. The $c\overline{c}$ pairs can evolve into heavier charmonium states $\chi_c$(1P) and $\psi$(2S) that undergo transitions into $J/\psi$(1S) mesons. The decay of the $\chi_c$(1P) states into $J/\psi$ and a single photon considered in this thesis is omitted in Fig. 1.4 for clarity. The respective quantum numbers $J^{PC}$ are also listed in Fig. 1.4.

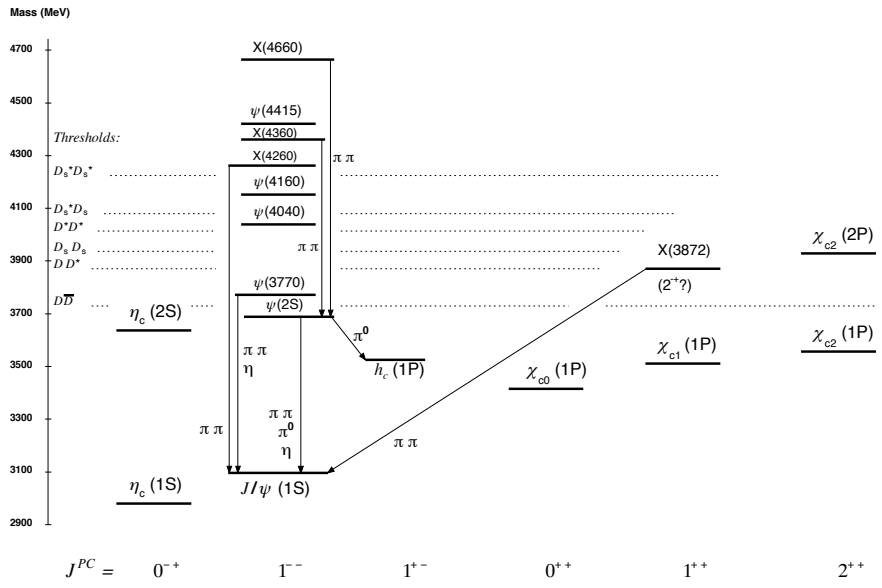


Figure 1.4: The level scheme of the $c\overline{c}$ states showing experimentally established states with solid lines. Only observed hadronic transitions are shown; the single photon transitions $\psi(nS) \rightarrow \gamma\eta_c(mS)$, $\psi(nS) \rightarrow \gamma\chi_{cJ}(1P)$ and $\chi_{cJ}(1P) \rightarrow \gamma J/\psi$ are omitted for clarity [7]

The properties of the $\chi_c$ states can be seen in Tab. 1.1. The $\chi_{c0}$ will be neglected in this thesis, since its branching fraction in the radiative decay to $J/\psi\gamma$ is only roughly 1%.

| | mass [GeV/$c^2$] | full width $\Gamma$ [MeV/$c^2$] | measured lifetimes [s] | $\mathcal{BR}$ [%] |
|---|---|---|---|---|
| $\chi_{c0}$ | 3.41475 | 18.8 ± 3.5 | $(6.095 \pm 0.339) \cdot 10^{-23}$ | 1.40 ± 0.05 |
| $\chi_{c1}$ | 3.51066 | 1.19 ± 0.21 | $(7.84 \pm 0.37) \cdot 10^{-22}$ | 34.3 ± 1.0 |
| $\chi_{c2}$ | 3.55620 | 1.97 ± 0.09 | $(3.341 \pm 0.153) \cdot 10^{-23}$ | 19.0 ± 0.5 |

Table 1.1: Selected $\chi_c$ properties; the branching ratio ($\mathcal{BR}$) refers to the radiative decay of $\chi_c \rightarrow J/\psi + \gamma$; numbers taken from [7]

The decay of $\chi_c$ to $J/\psi$ has been the subject of several studies. Measurements of the ratio of $\chi_c$ and $J/\psi$ help to understand the properties of the QGP. The radius of the $\chi_c$ is greater than of the $J/\psi$, i.e. the charm and anticharm are at a greater distance from one another which increases the probability of the $c\bar{c}$ pair to be separated in QGP.
The CDF collaboration measured the fraction of $J/\psi$ mesons originating from $\chi_c$ meson decays in pp collisions at $\sqrt{s} = 1.8$ TeV in 1997. The fraction including only prompt production was determined to be $\approx 30\%$ for $p_T^{J/\psi} > 4.0$ GeV/$c$ and $|\eta^{J/\psi}| < 0.6$ [8].
A more recent measurement from the LHCb collaboration in 2012 of the prompt cross section ratio of $\chi_c$ to $J/\psi$ in pp collisions at a centre-of-mass energy of $\sqrt{s} = 7$ TeV through the decay of $\chi_c \rightarrow J/\psi \rightarrow \mu_+\mu_-\gamma$, covering the $J/\psi$ transverse momentum range 2 – 15 GeV and rapidity range 2.0 – 4.5 can be seen in Fig. 1.5 [9]. The fraction of $J/\psi$ from $\chi_c$ at forward rapidity examined by LHCb is approximately between 10 and 35% for $2 < p_T < 15$ GeV/$c$ [9].

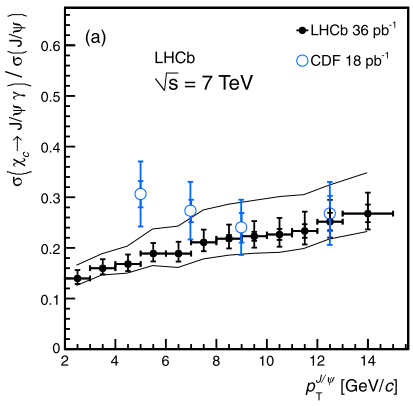


Figure 1.5: The fraction of $J/\psi$ mesons originating from $\chi_c$ meson decays in pp collisions at $\sqrt{s} = 7$ TeV [9]

The $\chi_c$ production and the relative amounts of the $\chi_{c1}$ and $\chi_{c2}$ spin states have previously been measured in pp collisions at various energy and $p_T$-ranges by ATLAS, LHCb and CMS. A selection of recent measurements in pp can be found e.g. in the following papers [10, 11, 12, 13]. Different proton nucleus collisions have been studied as well, see e.g. [14, 15].

So far, there are no existing measurements for PbPb collisions.

Based on a previous ALICE $J/\psi$ measurement and LHCb ratios of $\sigma(\chi_c)/\sigma(J/\psi)$ and $\sigma(\chi_{c2})/\sigma(\chi_{c1})$, this thesis aims to make predictions for the number of $\chi_{c1}$ and $\chi_{c2}$ mesons expected in pp collisions at $\sqrt{s} = 13$ TeV for ALICE in Run 3 for different integrated luminosities.

# Chapter 2

# The ALICE experiment and the upgraded ITS

ALICE (A Large Ion Collider Experiment) is one of the four big experiments at the Large Hadron Collider (LHC) at the European Organization for Nuclear Research (CERN, derived from Conseil Européen pour la Recherche Nucléaire), focusing on QCD. The main goal of the ALICE collaboration is to investigate the physical properties of the QGP, created under the extreme conditions of high temperature and energy density created in the nuclear-nuclear collisions at the LHC [16].

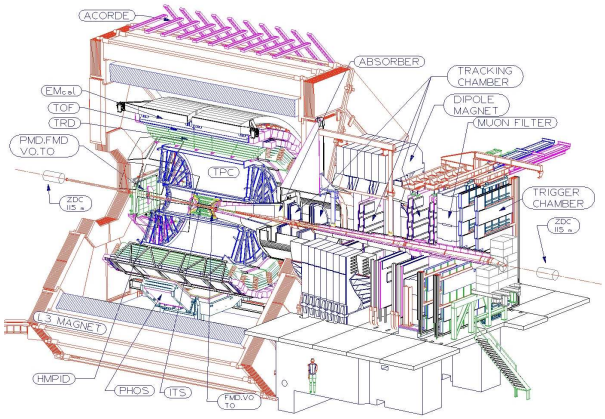


Figure 2.1: ALICE detector in Run 2 [16]

ALICE is made up of various detectors arranged in cylindrical shells around the interaction point (see Fig. 2.1), designed to determine the species and precise trajectory of the charged particles generated in the collisions. Each detector provides certain in-

formation in order to reconstruct the tracks and the energies of the produced particles and their decay products. The tracking system consists of the Inner Tracking System (ITS), which is located directly around the beam pipe, followed by the Time Projection Chamber (TPC) and the Transition Radiation Detector (TRD). They are part of the central barrel that is surrounded by the solenoid magnet, which is responsible for bending the tracks of charged particles.

Relevant for this study are the ITS and the TPC.
The TPC is the major tracking device and particle detector, providing continuous, three-dimensional tracking of charged particles between radii of 80 cm and 250 cm from the central interaction point [17].
The ITS determines the primary and secondary decay vertices of particle decays within a few millimetres to centimetres of the primary interaction point with high precision [18].

The ITS in LHC Run 2 consisted of six layers of silicon detectors surrounding the 1-mm-thick beam pipe enclosing the ultra-high vacuum of the accelerator. In 2021, the ITS was upgraded to ITS2 to improve the tracking precision, the tracking efficiency at low-transverse momenta and the readout rate capabilities.
The new ITS2 consists of seven concentric detector layers. A key feature of the new ITS2 is the very low mass of the three innermost layers. In comparison to the old ITS, the first layer in the new ITS2 is closer to the interaction point and the beam pipe radius and material budget are reduced [18]. A table comparing the key upgraded features from ITS and ITS2 can be found in the Appendix (A.1).

# Chapter 3

# Analysis: Outline

This chapter provides an overview of the content and method of this thesis.

The aim of this thesis is to calculate an estimated number of $\chi_{c1}$ and $\chi_{c2}$ mesons in pp collisions at $\sqrt{s}$ = 13 TeV for ALICE Run 3. For this, the $\chi_c$ mesons will be simulated based on real experimental measurements.

The kinematics of the $J/\psi$ have been widely studied and different ratios of prompt $\chi_c$ to $J/\psi$ and $\chi_{c1}$ to $\chi_{c2}$ production have been measured. Thus, the kinematics of the $\chi_{c1}$ and $\chi_{c2}$ mesons are calculated based on realistic $J/\psi$ measurements from pp collisions by the ALICE collaboration as well as ratios of the cross sections of $\chi_c$ to $J/\psi$ and $\chi_{c1}$ to $\chi_{c2}$ measured by LHCb. Additionally, in the Monte Carlo (MC) simulation, different kinematic selection criteria and efficiencies are applied analogously to the $J/\psi$ analysis. Finally, the estimated number of mesons at the integrated luminosity from Run 3 can be calculated.

The following chapters will give a detailed description of the different steps.
The kinematics of all included particles will be discussed in Chapter 4, Chapter 5 goes through the step-by-step effect of the selection criteria on the kinematic distributions and eventually the expected number of $\chi_c$ mesons will be presented in Chapter 7.

Later, the analysis is extended to present the effect of stricter selection criteria on the single leg cuts of the $J/\psi$ daughter tracks. Furthermore, the extrapolation of the $p_T^{J/\psi}$-distribution at low momenta in the not yet measured range $0 - 3$ GeV/$c$ and its effect on the expected number of the $\chi_c$ states will be discussed.
Finally, the effect of lepton transverse momentum smearing will be discussed in chapter 8, since the reconstructed invariant masses of the simulation are not realistic distributions obtained in an analysis of experimental data.

## 3.1 Monte Carlo simulation

The Monte Carlo simulation is done within the ALICE O2 framework [19]. One $\chi_{c0}$, $\chi_{c1}$ and $\chi_{c2}$ each are simulated per event.

The $\chi_c$ mesons decay to a $J/\psi$ and a photon via the radiative decay $\chi_c \rightarrow J/\psi + \gamma$. The $\chi_c$ mesons with the following PDG masses and Breit Wigner widths are listed in Tab. 3.1. (The full table can be found in the Appendix (A.3).)

| particle | mass [GeV/$c^2$] | width [GeV/$c^2$] |
|---|---|---|
| $\chi_{c0}$ | 3.41475 | $1.05 \cdot 10^{-2}$ |
| $\chi_{c1}$ | 3.51066 | $8.40 \cdot 10^{-4}$ |
| $\chi_{c2}$ | 3.55620 | $1.93 \cdot 10^{-3}$ |

Table 3.1: Mass and width of $\chi_c$ resonance [19]

The $J/\psi$ further decay to $e^+e^-$ or via the radiative decay ($e^+e^-\gamma$). The detector resolution and interaction with the detector material are disregarded.

The $\chi_c$ decays and $J/\psi$ decays in the dielectron channel are simulated with the EvtGen package [20]. The radiative decay of the $J/\psi$ is handled by PHOTOS [21]. A documentation of the decay table with the decay properties, i.e. the process of the decay, can be found in the Appendix (A.3).

## 3.2 Kinematics in collisions

To begin with, some basic kinematic concepts relevant for the considered collisions are introduced.

The relativistic energy $E$ and 3-momentum $\mathbf{p}$ of a particle of mass $m$ form a 4-vector

$$p^\mu = (E, \mathbf{p}),$$

referred to as 4-momentum. Both $E$ and $\mathbf{p}$ are separately conserved, hence the 4-momentum is also conserved. The scalar product of a 4-vector

$$p^\mu p_\mu = E^2 - \mathbf{p}^2 \tag{3.1}$$

is Lorentz-invariant, i.e. frame independent.
For a particle at rest, the 4-momentum $p^\mu = (m, \mathbf{0})$ and its Lorentz-invariant scalar product $p^\mu p_\mu = m^2$. Thus,

$$m^2 = E^2 - \mathbf{p}^2 \tag{3.2}$$

applies in all inertial frames.
For a system of $n$ particles, the squared invariant mass is equal to

$$p^{\mu}p_{\mu} = (\sum_{i=1}^{n} E_i)^2 - (\sum_{i=1}^{n} \mathbf{p}_i)^2. \tag{3.3}$$

In a particle decay, the invariant mass of the decay products equals the mass of the decaying particle [7, 1]. Hence, the invariant masses of the $J/\psi$ and $\chi_c$ mesons are calculated from their decay products $e^+$, $e^-$ and $\gamma$.

Another quantity to be introduced is the transverse momentum $p_T$, given as

$$p_T = \sqrt{p_x \cdot p_x + p_y \cdot p_y}, \tag{3.4}$$

where $x$ and $y$ describe the transverse plane in Fig. 3.1b. The detectors are surrounded by a solenoid magnet whose magnetic field bends the tracks of the particles in the $xy$-plane.

Finally, rapidity and pseudorapidity are introduced. In hadron collider experiments, the scattered partons are observed as jets. The angle of these jets with respect to the beam axis $z$ (described in Fig. 3.1a) are relatively well measured. These jet angles can be expressed in terms of rapidity $y$:

$$y = \frac{1}{2} \ln\left(\frac{E + p_z}{E - p_z}\right) \tag{3.5}$$

where $E$ and $p_z$ are the measured energy and longitudinal z-component of momentum of a jet.
For high energy jets, the jet mass is small compared to the energy ($m << E$) and the longitudinal momentum can be approximated by $p_z \approx E\cos\theta$. Here, $\theta$ describes the polar angle of the jet with respect to the beam axis and $\cos\theta = p_z/p$. The rapidity is then approximated by

$$y \approx \frac{1}{2} \ln\left(\frac{1 + \cos\theta}{1 - \cos\theta}\right) = \frac{1}{2} \ln\left(\cot^2 \frac{\theta}{2}\right) \tag{3.6}$$

This equals the pseudorapidity $\eta$ defined as

$$\eta = -\ln\left(\tan \frac{\theta}{2}\right) \tag{3.7}$$

So, for very high energies or negligible jet masses, the rapidity and pseudorapidity are approximately the same. In any case, $\eta$ can be measured when the mass and momentum of the particle are unknown [7, 1].

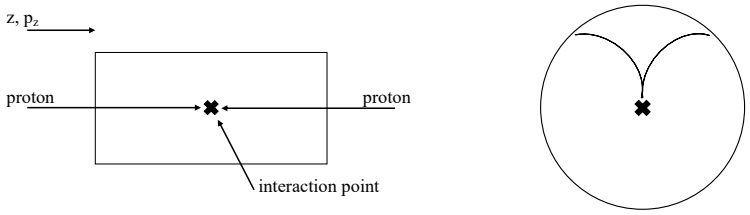


(a) Collision along the $z$ axis

(b) $xy$ - plane

Figure 3.1: Kinematics for collision along the beam axis, commonly denoted with $z$

# Chapter 4

# Analysis Part 1: $\chi_c$-Kinematics

This chapter discusses the kinematic derivations necessary for the simulation as well as the trends of the different kinematic distributions of the different particles.

## 4.1 Derivation of $\chi_c$ $p_T$-distributions

The $p_T$-distributions for the different $\chi_c$ mesons for the $\chi_c$-simulation are obtained through multiplications of the realistic $J/\psi$ $p_T$-distribution [5] with the ratios $R = \frac{\sigma(\chi_c)}{\sigma(J/\psi)}$ [9] and $R_{12} = \frac{\sigma(\chi_{c2})}{\sigma(\chi_{c1})}$ [11].

Neglecting $\chi_{c0}$ due to its small branching fraction (as discussed in Section 1.6) means that

$$\sigma(\chi_c) = \sigma(\chi_{c_1}) + \sigma(\chi_{c_2}) = \sigma(\chi_{c_1}) + R_{12} \cdot \sigma(\chi_{c_1}) \tag{4.1}$$

and therefore

$$\sigma(\chi_{c_1}) = \frac{1}{1+R_{12}} \cdot \sigma(\chi_c) \text{ and } \sigma(\chi_{c_2}) = \frac{R_{12}}{1+R_{12}} \cdot \sigma(\chi_c) \tag{4.2}$$

Substituting $p_T^{\chi_{ci}}$ for $\sigma(\chi_{ci})$ $(i = 1, 2)$ gives

$$p_T^{\chi_{c1}} = \frac{1}{1+R_{12}} \cdot p_T^{\chi_c} \text{ and } p_T^{\chi_{c2}} = \frac{R_{12}}{1+R_{12}} \cdot p_T^{\chi_c}. \tag{4.3}$$

Using $p_T^{\chi_c} = R \cdot p_T^{J/\psi}$ finally gives

$$p_T^{\chi_{c_1}} = \frac{R}{1+R_{12}} \cdot p_T^{J/\psi} \tag{4.4}$$

and

$$p_T^{\chi_{c_2}} = \frac{R}{1+\frac{1}{R_{12}}} \cdot p_T^{J/\psi} \tag{4.5}$$

In the following sections, the $J/\psi$ $p_T$-distributions obtained from measurements in pp collisions at $\sqrt{s} = 13$ TeV and midrapidity measured by ALICE [5] and the ratios from

LHCb measurements at $\sqrt{s} = 7$ TeV and forward rapidity [9, 11] will be discussed.
It is important to mention that the $p_T$-distribution of the $J/\psi$ is strongly dependent of the centre-of-mass energy. The $p_T$-distributions of the $\chi_c$ have a very similar energy dependence to that of the $J/\psi$ [22]. Thus, the ratios $R$ and $R_{12}$ are assumed to be independent of the beam energy and can be used in spite of the different centre-of-mass energy.
The invariant masses are reconstructed from the four-vectors of the respective decay products as discussed in Section 3.2

## 4.2 Inclusive $J/\psi$

The $p_T$-distributions for the $\chi_c$-simulation are calculated using the measured $p_T$-distributions for inclusive $J/\psi$ production in pp collisions at $\sqrt{s} = 13$ TeV [5].
The data used is from ALICE collaboration measurements of the inclusive $J/\psi$ production cross section in pp collisions at a centre-of-mass energy $\sqrt{s} = 13$ TeV, at midrapidity ($|y| < 0.9$) and using a minimum-bias data sample corresponding to an integrated luminosity $L_{int} = 32.2$ nb$^{-1}$. The $J/\psi$ mesons are reconstructed in the $e^+e^-$ decay channel.
A simple power law function of the type

$$f(p_T^{J/\psi}) = \frac{A \cdot p_T^{J/\psi}}{(1 + (\frac{p_T^{J/\psi}}{p_0})^2)^n} \tag{4.6}$$

with the parameters $A = 2.2855$, $p_0 = 3.73619$ and $n = 2.81708$ is used to fit the measured $p_T$-distribution.
The rapidity-distribution for the $J/\psi$ is a Gaussian distribution fitted to experimental data for the prompt $J/\psi$ in pp collisons at $\sqrt{s} = 13$ TeV for ALICE and LHCb at mid- and forward rapidity. The same Gaussian distribution is used for the $\chi_c$ mesons in the simulation.

## 4.3 Ratio of prompt $\chi_c$ to $J/\psi$ production

The ratio $R = \sigma(\chi_c \to J/\psi)/\sigma(J/\psi)$ seen in Fig. 4.1a is taken from the LHCb measurement of the ratio of cross sections for prompt charmonium $\chi_c$ to $J/\psi$ production in proton-proton interactions at a centre-of-mass energy of $\sqrt{s} = 7$ TeV. The $\chi_c$ mesons, from a data sample of integrated luminosity of 36 pb$^{-1}$ collected during 2010, are identified through their decay $\chi_c \to J/\psi \to \mu_+\mu_-\gamma$ covering the $J/\psi$ transverse momentum range $2 < p_T^{J/\psi} < 15$ GeV/$c$ and rapidity range $2.0 < y < 4.5$. Prompt production of $\chi_c$ refers to $\chi_c$ mesons that are produced directly, or indirectly via the decay of higher excited charmonium states and do not arise from the decay of a b-hadron [9].
The $p_T$-integrated value is given by

$$R = \frac{\sigma(\chi_c \to J/\psi)}{\sigma(J/\psi)} = 0.188 \pm 0.013\ (\text{stat})\ ^{+0.024}_{-0.022}\ (\text{syst})\ \ [9].$$

The linear approximation

$$R = 0.121 + 0.011 \cdot p_T^{J/\psi}$$

fitted to the LHCb data in Fig. 4.1b reweights the distributions used in the simulation.

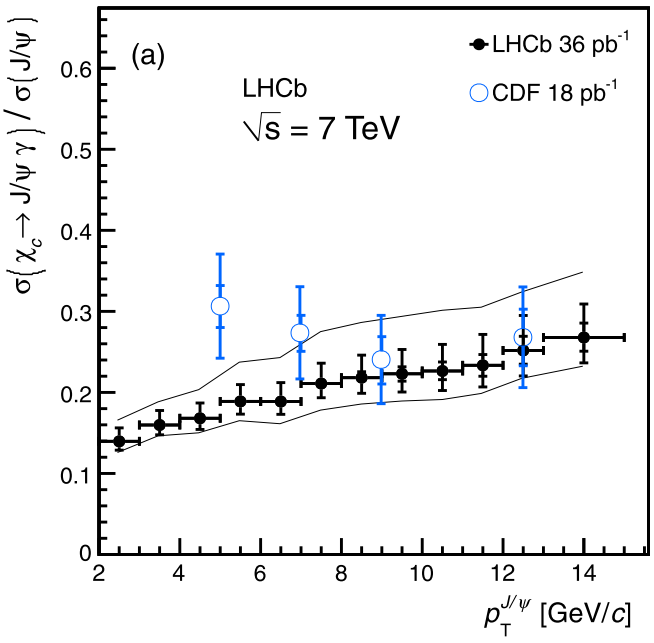


(a) Solid black circles: rapidity range $2.0 < y^{J/\psi} < 4.5$ and assuming the production of unpolarised $J/\psi$ and $\chi_c$ mesons; internal error bars: statistical error; external error bars: include systematic uncertainties (apart from polarisation); lines surrounding data points: show maximum effect of the unknown $J/\psi$ and $\chi_c$ polarisations; in blue: CDF data points, at $\sqrt{s} = 1.8$TeV in pp collisions and in the $J/\psi$ pseudo rapidity range $|\eta^{J/\psi}| < 1.0$ [9]

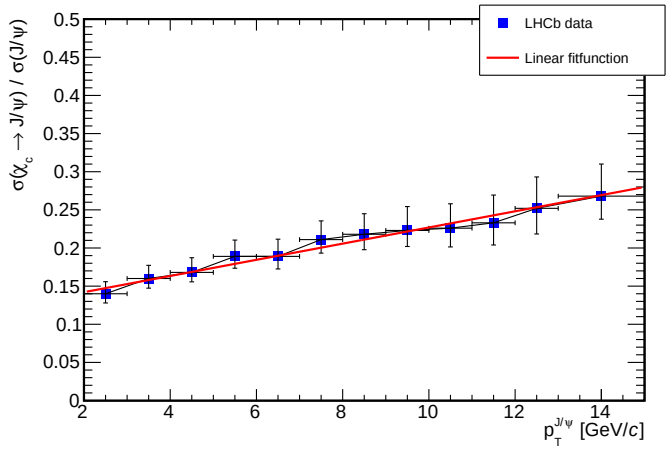


(b) Ratio fitted with linear polynomial $R = 0.121 + 0.011 \cdot p_T^{J/\psi}$ for simulation; the plot shows the data points and the squared sum of the statistical and systematic errors. The systematic errors regarding the polarization are not included; data from [23]

Figure 4.1: Both graphs show the same ratio $\sigma(\chi_c \to J/\psi)/\sigma(J/\psi)$ in bins of $p_T^{J/\psi}$ in the range $2 < p_T^{J/\psi} < 15$ GeV/$c$ as measured by the LHCb collaboration at $\sqrt{s} = 7$ TeV [9]

## 4.4 Ratio of prompt $\chi_{c2}$ to $\chi_{c1}$ production

The ratio $R_{12} = \sigma(\chi_{c2})/\sigma(\chi_{c1})$ shown in Fig. 4.2a is taken from the LHCb measurement of the prompt production of charmonium $\chi_{c0}$, $\chi_{c1}$, $\chi_{c2}$ mesons in pp collisions at a centre-of-mass energy of $\sqrt{s} = 7$ TeV. The $\chi_c$ mesons were identified through their radiative decay to $J/\psi\gamma$, with $J/\psi \to \mu_+\mu_-$ and photons that converted in the detector. A data sample, corresponding to an integrated luminosity of 1.0 fb$^{-1}$ collected by the LHCb detector, was used to measure the relative prompt production rate of $\chi_{c1}$ and $\chi_{c2}$ in the rapidity range $2.0 < y < 4.5$ as a function of the $J/\psi$ transverse momentum from $3 < p_T^{J/\psi} < 20$ GeV/$c$ [11].
The ratio of cross-sections of $\chi_{c1}$ and $\chi_{c2}$, integrated over $p_T^{J/\psi}$ is given by

$$R_{12} = \frac{\sigma(\chi_{c2})}{\sigma(\chi_{c1})} = 0.787 \pm 0.014\ (\text{stat}) \pm 0.034\ (\text{syst}) \pm 0.051\ (p_T\ \text{model}) \pm 0.047\ (\mathcal{BR})\ .$$

The first uncertainty is statistical, the second is the systematic uncertainty dominated by the photon efficiency, the $\chi_{c1}$ tail parameters and background modelling, the third is due to the choice of $p_T$-spectrum and the fourth is from the branching fraction uncertainty [11]. Similar to the linear fit of $R$ in Section 4.3, the $p_T$-differential ratio $R_{12}$ is fitted with the second degree polynomial approximation

$$R_{12} = 1.43953 - 0.145874 \cdot p_T^{J/\psi} + 0.00638469 \cdot (p_T^{J/\psi})^2$$

in Fig. 4.2b, which is used to reweight the distributions to then use them in simulations.

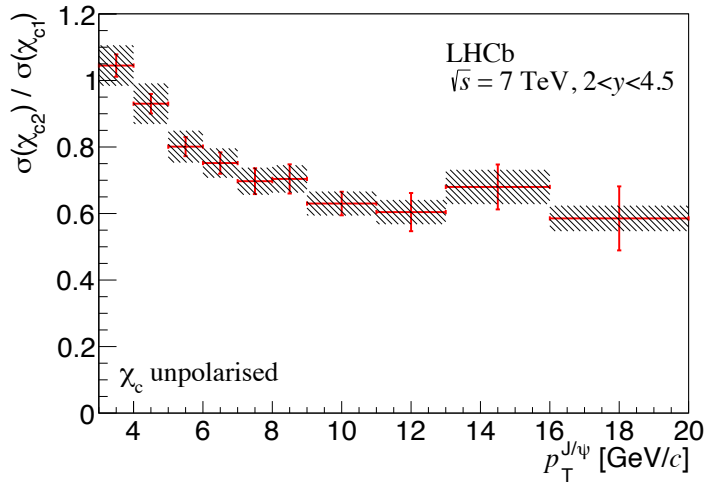


(a) The statistical uncertainty is shown with a red error bar and the systematic uncertainty with a hashed rectangle [11]

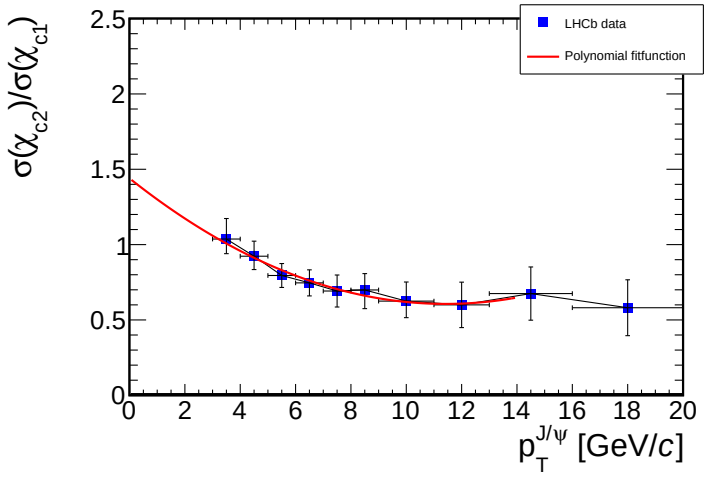


(b) Ratio fitted with 2nd degree polynomial $R_{12} = 1.43953 - 0.145874 \cdot p_T^{J/\psi} + 0.00638469 \cdot (p_T^{J/\psi})^2$ for simulation; data from [24]

Figure 4.2: Both graphs show the same ratio of $\sigma(\chi_{c2})/\sigma(\chi_{c1})$ in bins of $p_T^{J/\psi}$ in the range $4 < p_T^{J/\psi} < 20$ GeV/$c$ as measured by the LHCb collaboration at $\sqrt{s} = 7$ TeV for $2.0 < y < 4.5$. The plot shows the data points and the squared sum of the statistical and systematic errors. The systematic errors regarding the polarization are not included.

## 4.5 Kinematic distributions

This section presents relevant kinematic distributions. First, the kinematic distributions of the $\chi_c$ and $J/\psi$ mesons and thereafter those of the photons, leptons and antileptons are shown. At the end of this chapter, the opening angles of the different particles are discussed.

The $p_T$-distributions of the $J/\psi$ and $\chi_c$ mesons obtained according to the calculations in the previous Section 4.1 are shown in Fig. 4.3.
The difference in the $p_T^{\chi_{c1}}$ and $p_T^{\chi_{c2}}$ distributions is simply due to the factor $R_{12}$ in the relation $p_T^{\chi_{c1}} = R_{12} \cdot p_T^{\chi_{c2}}$. This approximated second degree polynomial $R_{12}$ is equal to unity at $p_T \approx 3.57$ GeV/$c$. As seen in Fig. 4.2, $R_{12}$ is greater than unity below and smaller than unity above this value. Thus, the $p_T^{\chi_{c2}}$ distribution is above the $p_T^{\chi_{cc1}}$ distribution in the range from zero up to $p_T \approx 3.57$ GeV/$c$ and then below for greater $p_T$.
The reweighting of $p_T^{J/\psi}$ with $R/(1+R_{12})$ for $p_T^{\chi_{c1}}$ (compare to Eq. 4.4) and $R/(1+1/R_{12})$ for $p_T^{\chi_{c2}}$ (compare to Eq. 4.4) result in the relations of the $p_T$-distributions of the $J/\psi$ and $\chi_c$ mesons seen in Fig. 4.3.

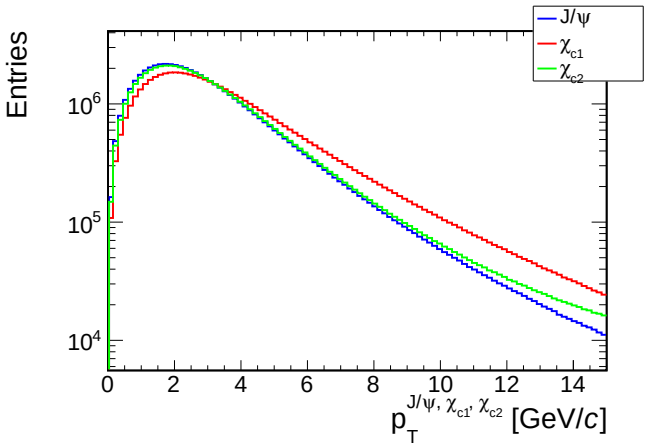


Figure 4.3: Simulated $p_T$-distributions of $J/\psi$, $\chi_{c1}$ and $\chi_{c2}$

The correlation of $p_T^{J/\psi}$ and $p_T^{\chi_{c1}}$ is shown in Fig. 4.4, the corresponding plot for $\chi_2$ can be found in Fig. A.3a in the Appendix. The transverse momenta of $\chi_{c1}$ and $J/\psi$ show a linear correlation. Since the $\chi_{c1}$ decays to $J/\psi$ and $\gamma$, $p_T^{J/\psi} < p_T^{\chi_{c1}}$. The correlation broadens at larger $p_T$, smearing downward.

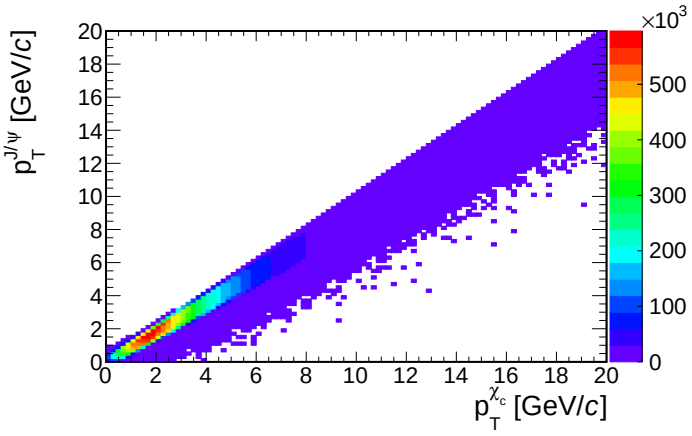


Figure 4.4: $p_T$-correlation of $\chi_{c1}$ and $J/\psi$

Fig. 4.5 shows the reconstructed invariant masses of $J/\psi$ and the $\chi_{c1}$ and $\chi_{c2}$ mesons, calculated according to Section 3.2. The peaks of the invariant masses are distinct and correspond to the measured masses. The width of the distributions comes from the Breit-Wigner distributions with the parameters listed in Tab. 1.1, the tails on the left of each peak are due to the radiative decays of the $J/\psi$.

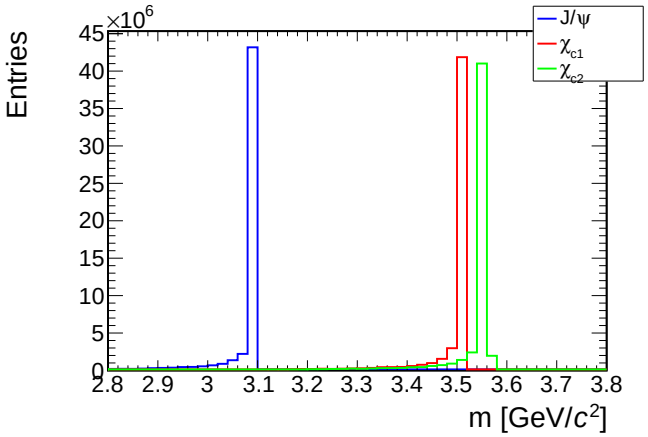


Figure 4.5: Reconstructed invariant masses of $J/\psi$, $\chi_{c1}$ and $\chi_{c2}$

The following discussion considers only the $\chi_{c1}$ and not the $\chi_{c2}$ meson, but it is exemplary for both since they show very similar trends. The corresponding $\chi_2$-distributions can be found in Figure A.7 in the Appendix.

The distributions of $\phi$ and $\theta$ of the $\chi_{c1}$ and $J/\psi$ in Fig. 4.6 are almost identical. The $\phi$-distributions for $\chi_{c1}$ and $J/\psi$ in Fig. 4.6a show that the angle in the $xy$-plane described in Fig. 3.1 is isotropically distributed across the whole $xy$-plane (range $(0, 2\pi)$). The $\theta$-distributions in 4.6b show the angle along the beam direction. The particles cover the whole range $(0, \pi)$ and most are deflected by $\sim \pi/4$ rad in either direction of the beam axis.

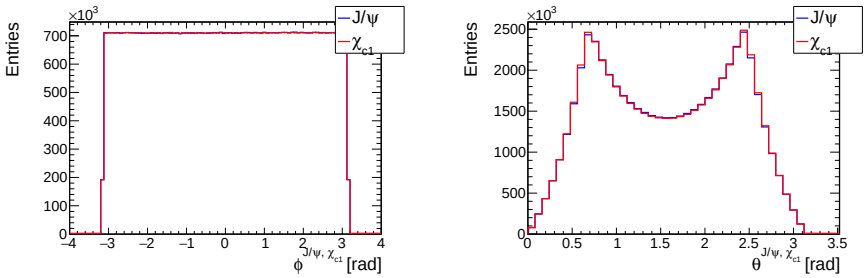


(a) Angle $\phi$ in $xy$-plane

(b) Angle $\theta$ along beam axis

Figure 4.6: Angular distributions of $\chi_{c1}$ and its corresponding $J/\psi$

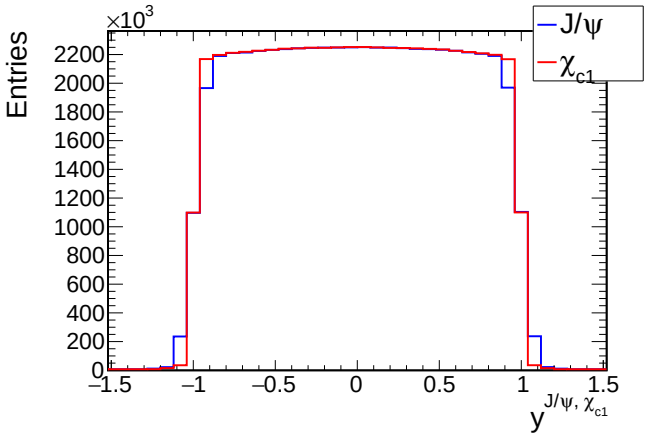


Figure 4.7: Rapidity distributions for $\chi_{c1}$ and its corresponding $J/\psi$

The Gaussian distributions in Fig. 4.7 show the predetermined rapidities introduced in Section 4.2. These are the distributions fitted to experimental data for the prompt $J/\psi$ in pp collisons at $\sqrt{s} = 13$ TeV for ALICE and LHCb at mid- and forward rapidity.

The following Figs. 4.8 and 4.9 show the kinematics for the photon on the left and lepton and antilepton on the right. Again, these plots belong to the $\chi_{c1}$ decay, the plots for the $\chi_{c2}$ can be found in Figs. A.4 and A.5 in the Appendix.
The $p_T$-distributions in 4.8 describe exponentially decreasing spectra. The majority of photons are found in the range below 1 GeV/$c$, most leptons and antileptons are in the range up to 4 GeV/$c$.

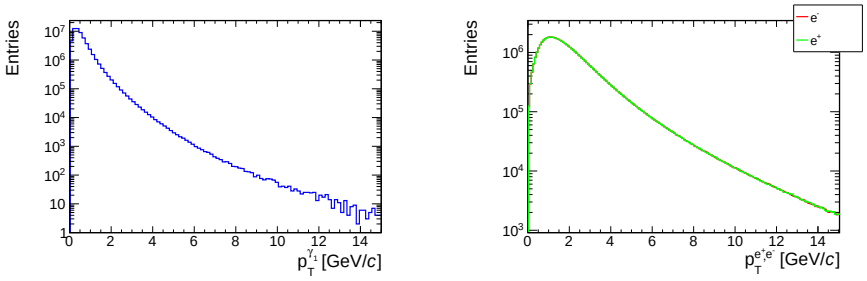


(a) $p_T$-distribution of photon

(b) $p_T$-distributions of lepton and antilepton

Figure 4.8: $p_T$-distributions of the photon from the $\chi_{c1}$ decay and leptons and antileptons from the corresponding $J/\psi$ decay

The $\phi$-distributions show that the photons and $e^+e^-$ are also isotropically distributed in the whole $xy$-plane (right in Fig. 3.1, range $(0, 2\pi)$). Figures 4.9e and 4.9f show the angle $\theta$ relative to the beam axis ($z$-axis in Fig. 3.1, range $(0, \pi)$). Theses distributions differ slightly from the $J/\psi$ and $\chi_c$ $\theta$-distributions in Fig 4.6b, there is no dip at $\pi/2$ rad, meaning that more of these lighter particles than mesons are not deflected. The rapidity (and in these cases of very light to massless particles also pseudorapidity) is simulated symmetrically as seen in Figs. 4.9a and 4.9b.

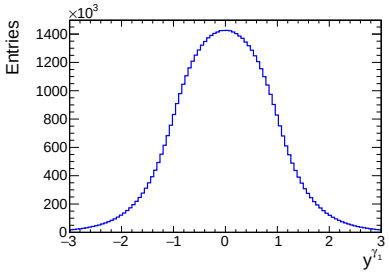


(a) $y$-distribution of photon

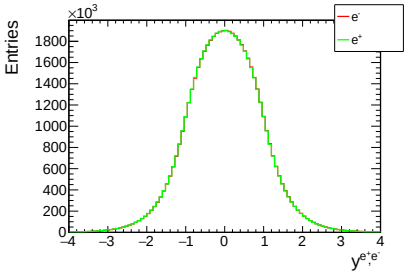


(b) $y$-distributions of lepton and antilepton

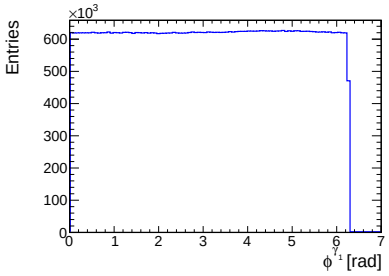


(c) $\phi$-distribution of photon

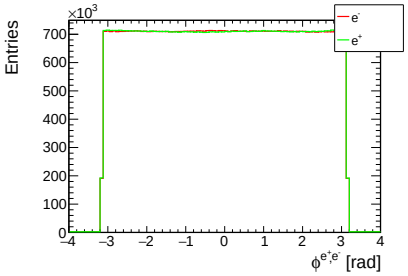


(d) $\phi$-distributions of lepton and antilepton

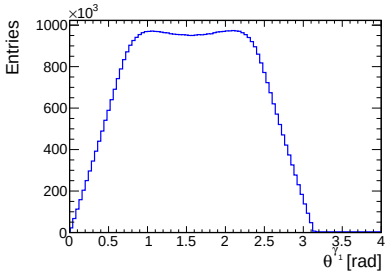


(e) $\theta$-distribution of photon

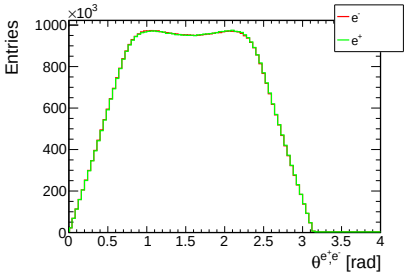


(f) $\theta$-distributions of lepton and antilepton

Figure 4.9: Kinematics of the photon from the $\chi_{c1}$ decay and leptons and antileptons from the corresponding $J/\psi$ decay

Further interesting distributions to be looked into are the opening angles between different particles. Particles should be separated enough to be easily detected and distinguished. Additionally, knowledge about the opening angles can be used to better reconstruct the decay and detect the correct electrons and positrons. The signal to background ratio could be improved in the analysis by introducing a selection criteria on the angle ranges of the particles. This could also be used as input for the machine

learning.

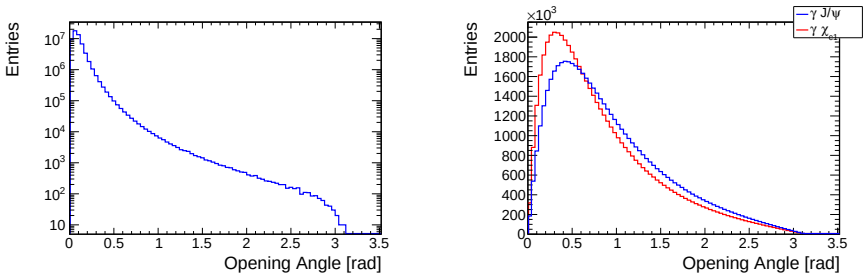


(a) Opening angle of $J/\psi$ and $\chi_{c1}$

(b) Opening angle of photon and $J/\psi$ as well as photon and $\chi_{c1}$

Figure 4.10: Opening angles for $\chi_{c1}$ and the corresponding $J/\psi$

On the one hand, the opening angles of the $J/\psi$ and $\chi_c$ mesons are similar, Fig.4.10a shows exactly this. Most events have very small to zero opening angles. Fig.4.10b shows the opening angle of the photon and the $J/\psi$ as well as the opening angle of the photon and the $\chi_c$. These two distributions are similar and both show that the $J/\psi$ or $\chi_c$ have non zero but nontheless very small opening angles with the photon.
On the other hand, the plots in Fig. 4.11a show that their decay products $e^+$ and $e^-$ have opening angles far greater than zero. Since these are the ones that are detected in the measurement, detection is possible.
The opening angles of photon and lepton as well as the opening angles of photon and antilepton in Fig. 4.11b show that these particles have opening angles greater than zero as well, meaning that all decay products travel in different enough directions to be detected separately. Fig. 4.11c shows the correlation of the opening angle of $e^+e^-$ and the transverse momentum of the $J/\psi$.

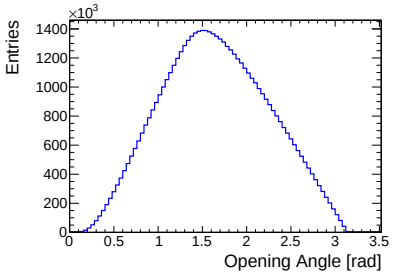


(a) Opening Angle of lepton and antilepton

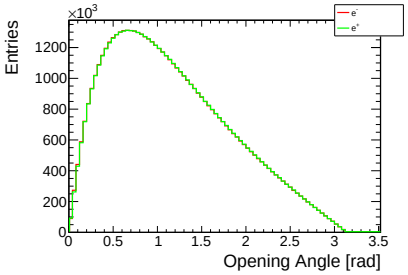


(b) Opening Angle of photon and lepton as well as photon and antilepton

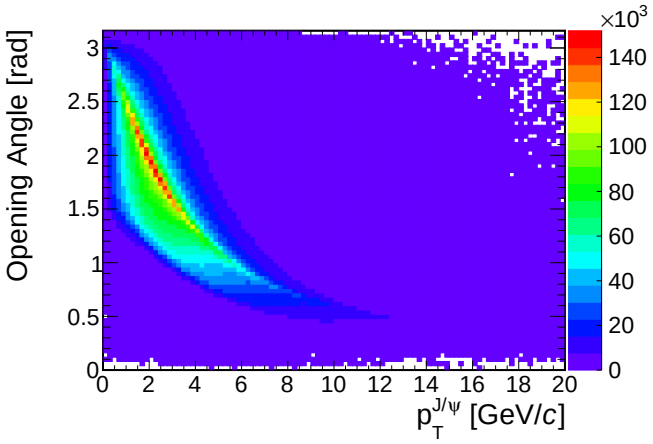


(c) Correlation of the opening Angle of lepton and antilepton and the transverse momentum of $J/\psi$ $p_T^{J/\psi}$

Figure 4.11: Different opening angles of lepton and antilepton from the $\chi_{c2}$ decay

# Chapter 5

# Analysis Part 2: Efficiencies

To calculate the $\chi_c$ reconstruction efficiency, several selection criteria are applied. The overall efficiency is then calculated as the quotient of the number of $\chi_c$ mesons after applying all criteria over the number of $\chi_c$ mesons with selected rapidities. This is explained below in more detail.

In a standard $J/\psi$ data analysis, the $J/\psi$ is reconstructed from the $e^+e^-$ candidates corresponding to the $J/\psi$ decay channel into an electron-positron pair or the radiative decay channel of which only the electron-positron pair is measured. Their tracks are reconstructed and detected in the ITS and the TPC. A track in the electron-positron pair is also referred to as a "single leg". In this $\chi_c$ analysis, the $J/\psi$ mesons are reconstructed analogously. Hence, the same selection criteria for the kinematic acceptance are applied. Further, the efficiency of a standard $J/\psi$ analysis in p-Pb collisions, i.e. a full MC simulation with particle transport through the detector and with track reconstruction, is implemented [25]. The requirements are summarised in Tab. 5.1.

| Cut number | Condition |
|---|---|
| 1 | $\chi_c$ rapidity $\lvert y_{\chi_c}\rvert < 0.9$ |
| 2 | Single leg cuts of $J/\psi$ daughter tracks: $p_T^e > 1$ GeV/$c$ and $\lvert y_e\rvert < 0.9$ |
| 3 | $J/\psi$ reconstruction efficiency |
| 4 | Photon efficiency |

Table 5.1: Selection Criteria applied in the simulation of the reconstructed $\chi_c$ mesons

The overall efficiency is then calculated as $\epsilon = \frac{\text{Entries after final Cut}}{\text{Entries after first Cut}}$.

## 5.1 Cut 1 - $\chi_c$ rapidity selection

As a kinematic cut the rapidity of the $\chi_c$ mesons is required to be $|y_{\chi_c}| < 0.9$ for each of the three $\chi_{c0}$, $\chi_{c1}$ and $\chi_{c2}$ mesons to ensure that the decay products are within the acceptance of the detector.

## 5.2 Cut 2 - Kinematic lepton acceptance

The single leg cuts of $J/\psi$ daughter tracks impose conditions on the transverse momentum and pseudorapidity of both lepton and antilepton. This step corresponds to the kinematic acceptance for each lepton.
Two conditions are required for the two leptons into which the $J/\psi$ decays. Firstly, it is required that the transversal momentum of the two legs is greater than 1 GeV/$c$. Following the Bethe-Bloch formula, the mean energy loss per distance of the electrons and hadrons is very similar in the TPC. They can be easily separated, i.e. the electrons are well detectable, at momenta greater than 1 GeV/$c$. Furthermore, it is required that the pseudorapidity of the two leptons is smaller than 0.9. The range of the used TPC detector responsible for electron identification is $-0.9 < \eta < 0.9$.

## 5.3 Cut 3 - $J/\psi$ efficiency

The radiative and non-radiative $J/\psi$ decays are reconstructed through $e^+$ and $e^-$. These pass the detector and interact with its material and are deflected in the magnetic field. The kinematics ($p_T$, $\eta$, $\phi$ etc) are reconstructed with the hit-information in the TPC. The invariant mass for real $J/\psi$ is calculated from the $e^+e^-$ pairs.

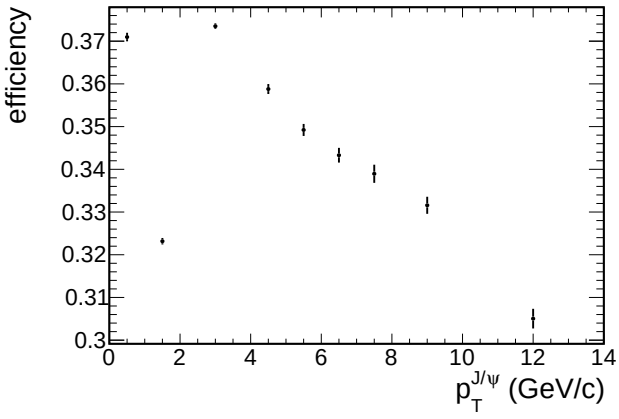


Figure 5.1: $J/\psi$ reconstruction efficiency [25]

The $J/\psi$ reconstruction efficiency, shown in Fig. 5.1, is taken from an analysis of p-Pb collisions at $\sqrt{s_{NN}}$ = 8.16 TeV taken in LHC Run 2 [25]. It includes the track reconstruction and electron identification of both leptons and is calculated as a function of transverse momentum.

## 5.4 Cut 4 - Photon efficiency

The inclusive photons are measured with the photon conversion method (PCM) with cuts that are also used in the neutral pion analysis. In the PCM (Fig. 5.2) the photons are detected through a photon conversion from $\gamma \rightarrow e^+e^-$ with a probability of $\approx 8.5\%$ in the detector material. The electron and positron $e^+e^-$ are tracked with the ITS and TPC detector and are identified with the TPC and TOF [26].

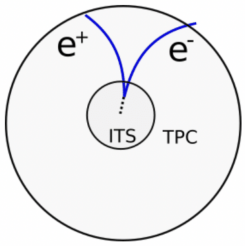


Figure 5.2: Photon Conversion Method [26]

The photon efficiency is calculated as the product of the corresponding photon reconstruction efficiencies and the conversion probabilities from the photon analysis in peripheral PbPb collisions at $\sqrt{s_{NN}} = 5.02$ TeV taken in LHC Run 2 [26, 27].
The conversion probabilities (Fig. 5.3a) were calculated as the number of converted primary photons, divided by the number of all generated primary photons. It is determined by the amount and composition of detector material. The reconstruction efficiencies (Fig. 5.3b) were calculated as the number of validated reconstructed primary photons, divided by the number of all generated and converted primary photons. Both reconstruction efficiency and conversion probability are shown as a function of the true photon $p_T$ (instead of the reconstructed $p_T$) for a centrality class of 60-80%.

Despite the reduced material budget in the upgraded ITS2 in Run 3 (see Section 2), the conversion probability is similar in both Run 2 and Run 3. This was investigated in first MC simulations [28]. Within the scope of this thesis the conversion probability (and reconstruction efficiency) will thus be assumed to be the same for both runs [26].

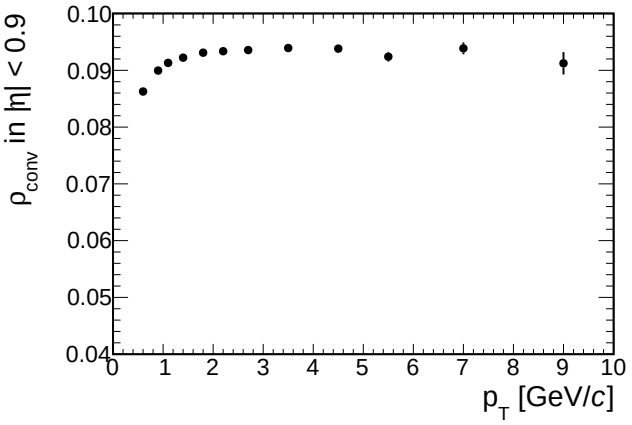


(a) Photon conversion probability

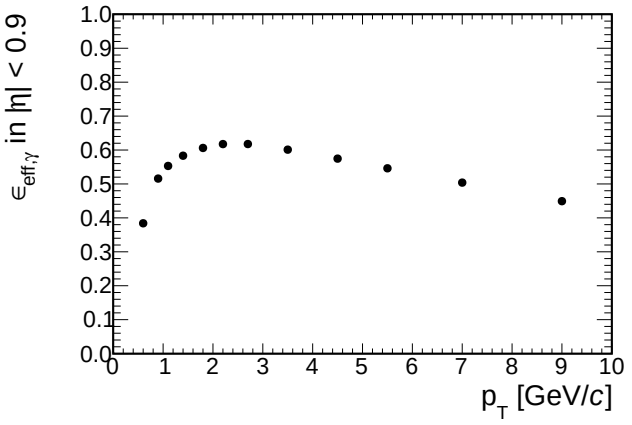


(b) Photon reconstruction efficiency

Figure 5.3: The photon reconstruction efficiency and the conversion probability from the photon analysis in peripheral PbPb collisions at $\sqrt{s_{NN}}$ = 5.02 TeV taken by ALICE in LHC Run 2 [26]

## 5.5 Effect of selection criteria and Efficiency

This section shows the effect of the applied selection criteria discussed above and the overall efficiencies obtained.

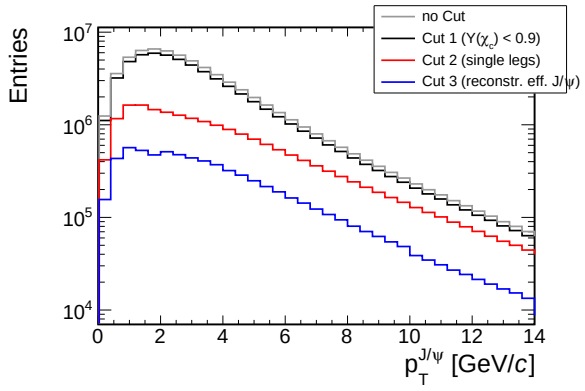


(a) on $J/\psi$

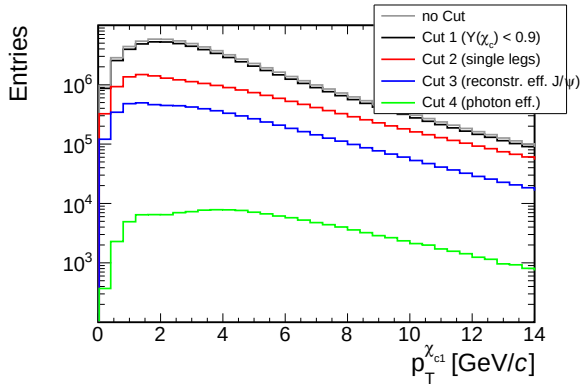


(b) on $\chi_{c1}$

Figure 5.4: Effects of applied selection criteria

The step by step effects of the selection criteria on the $p_T$-distributions of $J/\psi$ and $\chi_{c1}$ are shown in Fig. 5.4. The effect on $\chi_{c2}$ can be found in Fig. A.6 in the Appendix. The number of particles decrease drastically. Figure 5.5 shows the ratios of the different cuts, i.e. the effect of one cut to its previous one, comparing $J/\psi$ and $\chi_{c1}$ in Fig. 5.5a and $\chi_{c1}$ and $\chi_{c2}$ in Fig. 5.5b. The overall efficiencies as ratios of the final and first cuts are shown in Fig. 5.6.

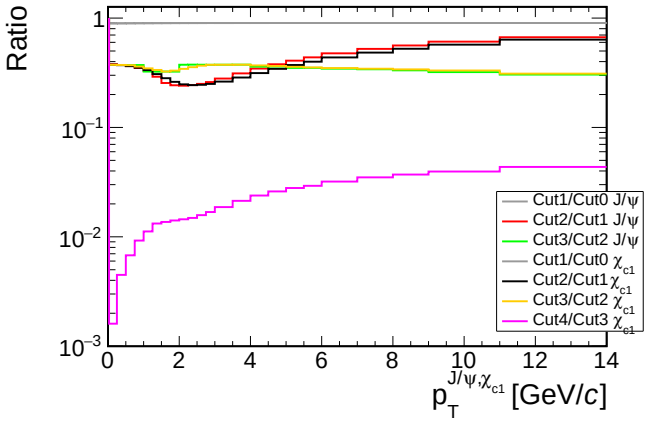


(a) Ratios of $J/\psi$ and $\chi_{c1}$ cuts

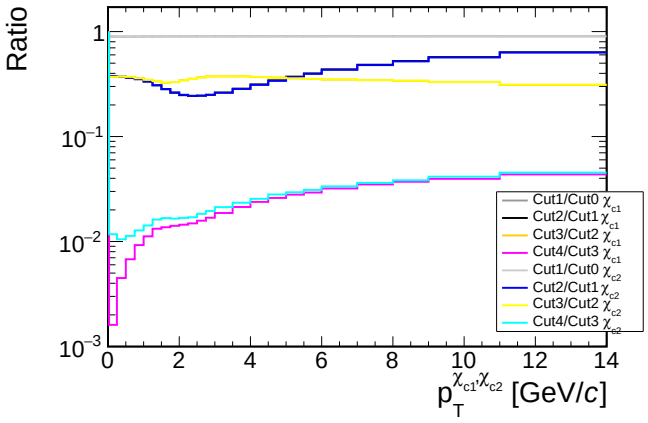


(b) Ratios of $\chi_{c1}$ and $\chi_{c2}$ cuts

Figure 5.5: The ratios of the different cuts for $J/\psi$ and the $\chi_c$ mesons

Figure 5.5a shows that applying Cut 1 on the rapidity of the mother particle $|y_{\chi_{ci}}| < 0.9$ ($i = 1, 2$) doesn't matter much, because not many $\chi_c$ exceed $|y_{\chi_c}| < 0.9$. The ratio of Cut1/Cut0 is 90% and constant.

The ratio of Cut2/Cut1 shows the effect of the kinematic acceptance, i.e. the minimum transverse momentum $p_T^e > 1$ GeV/$c$ and the cut on the pseudorapidity of the leptons $|y_e| < 0.9$. The single leg cuts show a $p_T$-dependence: the leptons from the decayed $J/\psi$ have different high and low momenta, which explains the rise of both sides of the

minimum around 2.5 GeV/$c$. Further, the single leg cuts seem to have slightly different effects on the $J/\psi$ and $\chi_c$ mesons, which is mainly explainable by the photon included in the $\chi_c$ but not the $J/\psi$ reconstruction. Partly, the slight difference of the $p_T^{J/\psi}$- and $p_T^{\chi_c}$-scales could also have an effect. However, as seen in Fig. 4.4, the $p_T^{J/\psi}$ and $p_T^{\chi_c}$ are linearly correlated and close enough to be considered equal for the sake of this exercise.

The ratio of Cut3/Cut2 is the applied $J/\psi$ reconstruction efficiency, which is the same for $J/\psi$, $\chi_{c1}$ and $\chi_{c2}$. This efficiency, unlike the single leg cuts, is hardly dependent of the momentum. The $J/\psi$ reconstruction efficiency as a function of $p_T$ is around 32-37% and relatively flat. This weak $p_T$-dependence results in alomst the same effects on the $\chi_c$ mesons.
Figures 5.5a and 5.5b show that Cuts 2 and 3 reduce the number of particles by roughly a factor of three.

The applied photon reconstruction efficiency and conversion probability in Cut 4 have the most drastic effect and reduces the overall efficiency of the respective $\chi_c$ states to roughly 0.2% (Fig. 5.6). While all cuts so far had exactly the same effects on $\chi_{c1}$ and $\chi_{c2}$ (All ratios except Cut4/Cut3 in Fig. 5.5b overlap completely), Cut 4 shows different effects on the 2 mesons: The different masses of $\chi_{c1}$ and $\chi_{c2}$ result in slightly different $p_T$-distributions for the photons of each meson (see Fig. 5.7a), so the photon reconstruction efficiency and photon conversion probabilities have slightly different effect on the two. Figure 5.7b compares the $p_T$-distributions of the photons from $\chi_{c1}$ and $\chi_{c2}$ after applying Cuts 3 and 4

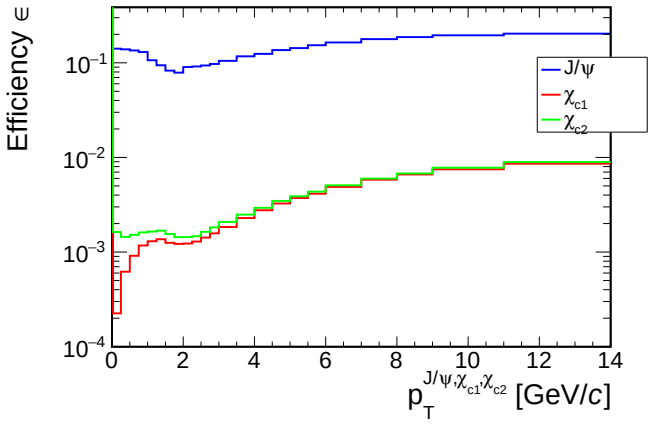


Figure 5.6: The overall efficiencies for $J/\psi$, $\chi_{c1}$ and $\chi_{c2}$, calculated by dividing the respective $p_T$-distributions after applying all cuts by the distribution after applying only the first cut on the rapidity range of the mother particles

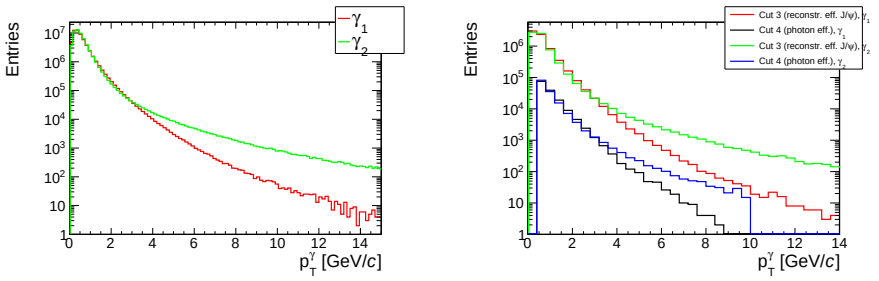


(a) $p_T$-distributions of the photons from $\chi_{c1}$ and $\chi_{c2}$ before applying any Cuts

(b) $p_T$-distributions of the photons from $\chi_{c1}$ and $\chi_{c2}$ after applying Cuts 3 and 4

Figure 5.7: Differences in the $p_T$-distributions of the photons from $\chi_{c1}$ and $\chi_{c2}$ before and after applying the Photon conversion probability and Photon reconstruction efficiencies to discuss the effect on the differences in the overall $\chi_{c1}$ and $\chi_{c2}$ efficiencies

For the $J/\psi$, the overall efficiency is calculated as

$$\epsilon_{J/\psi} = \frac{\text{Entries after Cut 3}}{\text{Entries after Cut 1}},$$

since the photon reconstruction and conversion probability of Cut 4 is not applied to the $J/\psi$. The overall efficiency of $\chi_{c1}$ and $\chi_{c2}$ is calculated as

$$\epsilon_{\chi_c} = \frac{\text{Entries after Cut 4}}{\text{Entries after Cut 1}}.$$

These overall efficiencies can also be understood as a product of all ratios shown in Figs. 5.5a and 5.5b, which explains the more or less smooth shape for the overall $J/\psi$ and $\chi_c$ efficiencies (shown in Fig. 5.6). Because the overall $J/\psi$ efficiency does not include the photon reconstruction and conversion probability, the overall $J/\psi$ efficiency indicates a minimum slightly more distinctive that in the efficiencies of $\chi_{c1}$ and $\chi_{c2}$ and is shifted as an effect of the sequence of multiplication. They all show slightly different $p_T$-dependencies.

The efficiencies of the $J/\psi$ at 1 and 5 GeV/$c$ are $\sim$ 20% and $\sim$ 30% at 10 GeV/$c$. The minimum at $\sim$ 2 GeV/$c$ is below 20%. Since the efficiency is $p_T$-dependent, the $p_T$-spectrum must be considered. More entries at smaller $p_T$ result in an overall integrated efficiency of $\sim$ 10%.
The efficiencies of the $\chi_{c1}$ and $\chi_{c2}$ after Cut 4 are both below 1%, reaching $\sim$ 0.8% at 10 GeV/$c$. The efficiencies at 5 GeV/$c$ are both roughly 0.3% and both roughly 0.2% at 5 GeV/$c$. The $\chi_{c1}$ dip for very low $p_T$ goes down to almost 0.02%.

# Chapter 6

# Analysis Part 3: Expected number of $\chi_c$ mesons

This chapter explains how the estimated number of $\chi_{c1}$ and $\chi_{c2}$ particles is calculated and discusses the necessary luminosities and cross sections.

## 6.1 Calculation method

The number $n_{\chi_c}$ for each of the $\chi_{c1}$ or $\chi_{c2}$ mesons is given by

$$n_{\chi_c} = \epsilon_{\chi_c} \cdot \sigma_{\chi_c} \cdot \int \mathcal{L}\,\mathrm{dt} \tag{6.1}$$

for a given integrated luminosity $\mathcal{L}$ (discussed in more detail in the following Section 6.2), $\epsilon_{\chi_c}$ are the final efficiencies for $\chi_{c1}$ and $\chi_{c2}$ calculated in 5.5 and $\sigma_{\chi_c}$ are the corresponding cross sections for $\chi_{c1}$ and $\chi_{c2}$ (derived from the $J/\psi$ cross section which is discussed in Section 6.3).
The cross section of all $\chi_c$ mesons decaying to $J/\psi$ is given by

$$\sigma(\chi_c \to J/\psi) = R \cdot \sigma(J/\psi) \tag{6.2}$$

where $R = \sigma(\chi_c \to J/\psi)/\sigma(J/\psi)$ is the ratio of prompt $\chi_c$ to $J/\psi$ production discussed in Sectionion 4.3. The cross section of all $\chi_c$ mesons decaying to $J/\psi$ is also given by the average branching ratio $\overline{BR}$ of $\chi_{c1}$ and $\chi_{c2}$ multiplied by the total $\chi_c$ cross section $\sigma(\chi_c)$:

$$\sigma(\chi_c \to J/\psi) = \overline{BR} \cdot \sigma(\chi_c) \tag{6.3}$$

Here, the average branching ratio $\overline{BR}$ is given by

$$\overline{BR} = \frac{\sigma(\chi_{c_1})}{\sigma(\chi_c)} B_1 + \frac{\sigma(\chi_{c_2})}{\sigma(\chi_c)} B_2 = \frac{1}{1 + R_{12}} \cdot (B_1 + R_{12} \cdot B_2) \approx 27.6\% \tag{6.4}$$

where $B_1$ and $B_2$ are the branching ratios of $\chi_{c1}$ and $\chi_{c2}$ respectively from Tab. 1.1. $R_{12} = \sigma(\chi_{c2})/\sigma(\chi_{c1})$ is the ratio of prompt $\chi_{c2}$ to $\chi_{c1}$ production discussed in Section.

4.4.
Equations 6.2 and 6.3 result in the total $\chi_c$ cross section $\sigma(\chi_c)$

$$\sigma(\chi_c) = \frac{R}{\overline{BR}} \cdot \sigma(J/\psi) \tag{6.5}$$

Using the formulas in Eq. 4.3 for $\sigma(\chi_{c_1})$ and $\sigma(\chi_{c_2})$ as functions of $\sigma(\chi_c)$ and using $\sigma(\chi_{ci} \to J/\psi) = \overline{B_i} \cdot \sigma(\chi_{ci})$ (i = 1,2) as well as Eq. 6.5, the respective $\chi_{c1}$ and $\chi_{c2}$ cross sections are given by:

$$\Rightarrow \sigma(\chi_{c_1} \to J/\psi) = B_1 \frac{R}{\overline{BR}} \frac{1}{1 + R_{12}} \sigma(J/\psi) \tag{6.6}$$

$$\Rightarrow \sigma(\chi_{c_2} \to J/\psi) = B_2 \frac{R}{\overline{BR}} \frac{R_{12}}{1 + R_{12}} \sigma(J/\psi) \tag{6.7}$$

## 6.2 ALICE pp physics programme in LHC Run 3

The expected number of $\chi_{c1}$ and $\chi_{c2}$ mesons is calculated for different scenarios in this thesis. The first running scenario are minimum bias pp collisions at an integrated luminosity of 2 pb$^{-1}$ in LHC Run 3.
The second scenario is pp collisions analysed at 200 pb$^{-1}$ in Run 3 where only events with detected $J/\psi$ mesons are stored [29]. The $J/\psi$ mesons are identified with the same selection criteria applied in this thesis.

## 6.3 $J/\psi$ cross section

The $J/\psi$ cross section used for the calculation of the estimated number of $\chi_c$ mesons described in the previous Section 6.1 is the ALICE measurement of the inclusive $J/\psi$ production cross section measured in pp collisions at a centre-of-mass energy $\sqrt{s}$ = 13 TeV [5]. In that measurement, the $J/\psi$ mesons are reconstructed in the $e^+e^-$ decay channel and the measurements are performed at midrapidity ($|y| < 0.9$) in the transverse-momentum interval $0 < p_T < 40$ GeV/$c$, using a minimum bias data sample corresponding to an integrated luminosity $L_{int}$ = 32.2 nb$^{-1}$ . The $p_T$-integrated $J/\psi$ production cross section at midrapidity, measured using the minimum bias data sample, is

$$\frac{d\sigma(J/\psi)}{dy}|_{y=0} = 8.97 \pm 0.24 \text{ (stat)} \pm 0.48 \text{ (syst)} \pm 0.15 \text{ (lumi)} \ \mu\text{b [6]}$$

The systematic uncertainties of the $p_T$-differential cross section vary with bin number. For the final calculation the $p_T$-differentiated approximation described by the graph in Fig. 6.1 and the simple power law function

$$\frac{2.16 p_T}{(1 + (\frac{p_T}{4.052})^2)^3} \tag{6.8}$$

in the range (0,20) GeV/$c$ is used.

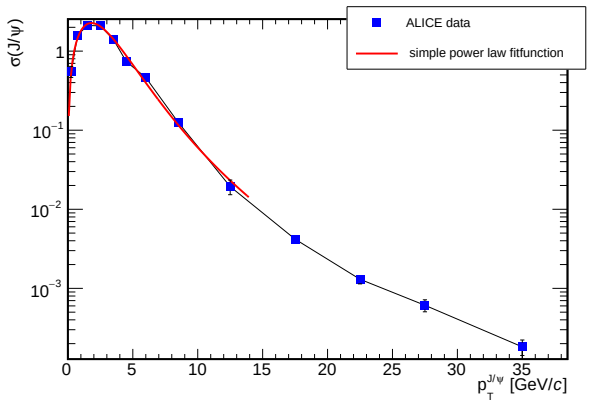


Figure 6.1: The $p_T$-differential cross section $\sigma(J/\psi)$ measured by the ALICE collaboration in pp collisions at a centre-of-mass energy $\sqrt{s}$ = 13 TeV [6]

The $\chi_{c1}$ and $\chi_{c2}$ cross sections are then calculated as described in the previous Section 6.1.

# Chapter 7

# Results

This chapter presents the key results of this thesis. First, the estimated number of $\chi_c$ mesons is presented. In addition to that, the analysis was extended further, and the effect of different single leg selection criteria, different extrapolations of the cross section ratio $R_{12}$ of $\chi_{c2}/\chi_{c1}$ to low momenta and single electron momentum smearing are discussed.

## 7.1 Estimated number of $\chi_c$ mesons

The estimated $p_T$-integrated numbers of detected $\chi_{c0}$, $\chi_{c1}$ and $J/\psi$ at an integrated luminosity of 2 pb$^{-1}$ are presented in Tab. 7.1. This integrated luminosity of 2 pb$^{-1}$ is the originally foreseen integrated luminosity of pp collisions in LHC Run 3 and 4 for ALICE. The determined values correspond to the $p_T$-integrated values calculated according to Eq. 6.1. The values given are the expected values after the corresponding analysis cuts and without efficiency correction, i.e. using the overall $J/\psi$ efficiency for Cut 3 of and the overall $\chi_c$ efficiency for Cut 4 (see Section 5.5).

| $J/\psi$ | $\chi_{c1}$ | $\chi_{c2}$ |
|---|---|---|
| $2.01 \cdot 10^6$ | 4260 | 2430 |

Table 7.1: The expected $p_T$-integrated numbers of $J/\psi$, $\chi_{c1}$ and $\chi_{c2}$ at an integrated luminosity of 2 pb$^{-1}$; the overall efficiencies $\epsilon_{J/\psi} = \frac{\text{Entries after Cut 3}}{\text{Entries after Cut 1}}$ and $\epsilon_{\chi_c} = \frac{\text{Entries after Cut 4}}{\text{Entries after Cut 1}}$ discussed in Section 5.5 are used

The $p_T$-differential distributions are shown in Fig. 7.1. The histograms are the respective overall efficiencies from Fig. 5.6 multiplied with the corresponding cross sections calculated in Section 6.1 and the constant integrated luminosity of 2 pb$^{-1}$.
The shape of the $p_T$-differential distributions of $\chi_{c1}$ and $\chi_{c2}$ are ascribed to the used ratios discussed in Sections 4.3 and 4.4 and overall efficiencies in Fig. 5.6 following the different selection criteria applied to the decay products of the $\chi_c$ mesons in Chapter 5.

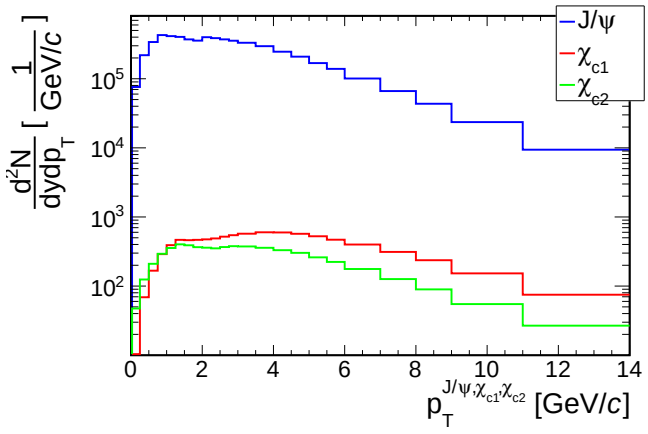


(a) Estimated number of $J/\psi$, $\chi_{c1}$ and $\chi_{c2}$

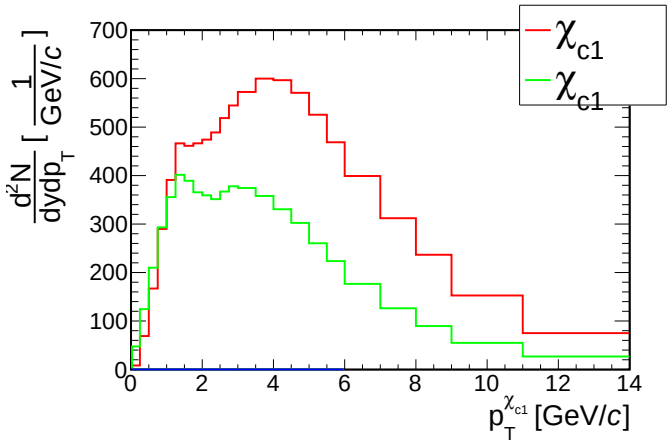


(b) Estimated number of $\chi_{c1}$ and $\chi_{c2}$

Figure 7.1: $p_T$-differential estimated numbers of $J/\psi$, $\chi_{c1}$ and $\chi_{c2}$ at an integrated luminosity of 2 pb$^{-1}$; the $p_T$-scale is for the corresponding meson

The estimated number of particles is linearly proportional to the integrated luminosity shown in Fig. 7.2. Thus, increasing the luminosity to e.g. 2 pb$^{-1}$ by a factor of 100 simply increases the estimated number of $\chi_c$ mesons by a factor of 100.

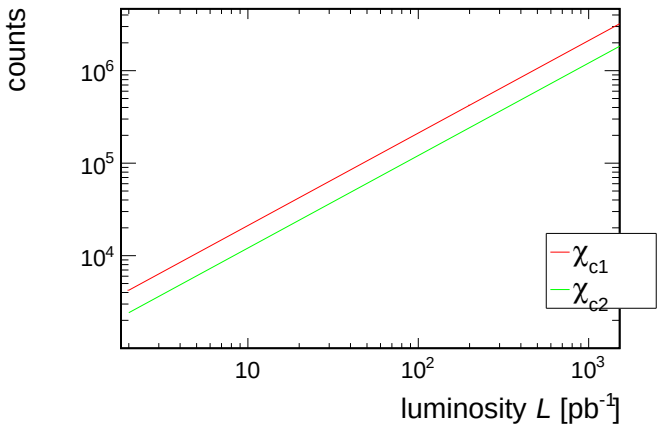


Figure 7.2: Estimated number of $\chi_{c1}$ and $\chi_{c2}$ mesons as a function of integrated luminosity $\mathcal{L}$

To motivate a search in experimental data, the $p_T$-integrated expected numbers should be no less than 500. This is attained at an integrated luminosity $\sim 0.25$ pb$^{-1}$ for the $\chi_{c1}$ mesons and $\sim 0.4$ pb$^{-1}$ for the $\chi_{c2}$ mesons.
Further, it is interesting to mention that far more $\chi_{c2}$ than $\chi_{c1}$ mesons are measured at low $p_T$ up to 4 GeV/$c$. More precisely, 170 $\chi_{c2}$ mesons and 130 $\chi_{c1}$ mesons are measured in the $(0, 1)$ GeV/$c$ $p_T$-range at a luminosity of 2 pb$^{-1}$.

## 7.2 Effect of different ratios of prompt $\chi_{c2}$ to $\chi_{c1}$ production

This section studies the extrapolation of the $\chi_{c2}/\chi_{c1}$ ratio.
The polynomial approximation described in Section 4.4 was used for the simulations in this thesis. This second degree polynomial (red function in Fig. 7.3) describes the data well in the range $3 - 14$ GeV/$c$ and is then used to extrapolate to zero $p_T$.

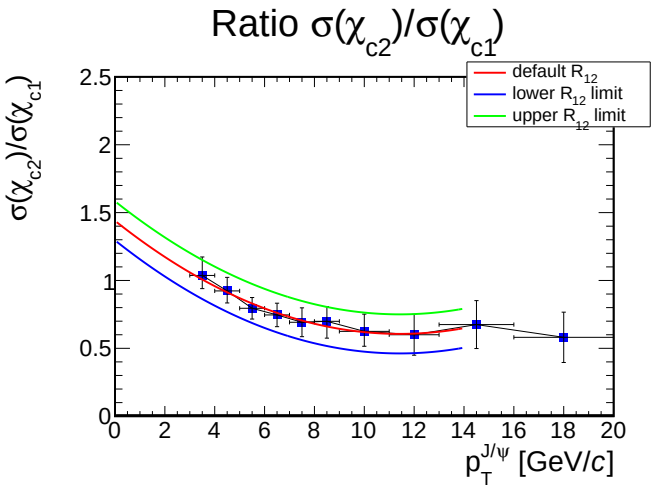


Figure 7.3: $R_{12}$ extrapolation

To calculate upper and lower estimates, the fit function is shifted up and down by a constant value of 10%. This value is obtained from the $p_T^{J/\psi}$-integrated cross section from 3 to 20 GeV/$c$ (see Section 4.4) [11]:

$\sigma(\chi_{c2})/\sigma(\chi_{c1}) = 0.787 \pm 0.014$ (stat) $\pm 0.034$ (syst) $\pm 0.051$ ($p_T$ model) $\pm 0.047$ ($\mathcal{BR}$) .

and is a conservative estimate as the quadratic sum of all uncertainties of the $p_T$-integrated cross section divided by the absolute value.
The effect of the upper and lower limit on the $p_T$-differential estimates can be seen in Fig. 7.4 and the corresponding $p_T$-integrated numbers are listed in Tab. 7.2. It is clearly visible that the upper limit for $R_{12} = \sigma(\chi_{c2})/\sigma(\chi_{c1})$ increases the $\chi_{c2}$ counts and decreases the $\chi_{c1}$ counts (green plots in 7.4), which is exactly opposite for the lower limit (blue plots).
The upper and lower estimates through the shifted fit function both show deviations of 5.4% for the expected $p_T$-integrated numbers of $\chi_{c1}$ relative to the default. The lower $R_{12}$-limit decreases the $p_T$-integrated estimated number of $\chi_{c2}$ mesons by roughly 11.5%. The upper limit increases the default estimate by 9.5%.

| Ratio | $\chi_{c1}$ | $\chi_{c2}$ |
|---|---|---|
| default $R_{12}$ | 4260 | 2430 |
| lower $R_{12}$ limit | 4490 | 2150 |
| upper $R_{12}$ limit | 4030 | 2660 |

Table 7.2: The expected $p_T$-integrated numbers at a luminosity of 2 pb$^{-1}$ for $\chi_{c1}$ and $\chi_{c2}$ for different Ratios of $R_{12}$

In this thesis, these upper and lower estimates through the shifted ratio of prompt $\chi_{c2}$ to $\chi_{c1}$ production are used as the overall estimated systematic uncertainties.

The final results are:

$$n_{\chi_{c1}} = 4260 \pm 230 \text{ (syst)}$$

$$n_{\chi_{c2}} = 2430\ ^{+230}_{-280} \text{ (syst)}$$

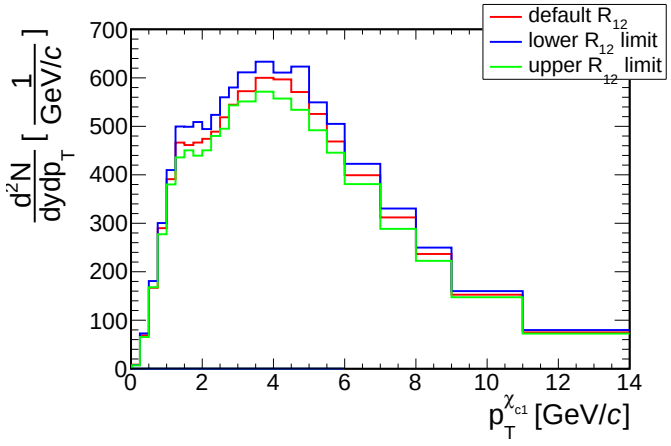


(a) $\chi_{c1}$

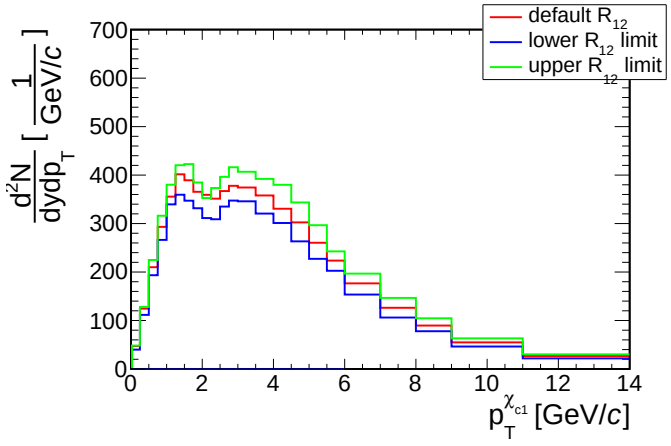


(b) $\chi_{c2}$

Figure 7.4: $p_T$-differential estimated numbers of $\chi_{c1}$ and $\chi_{c2}$ at an integrated luminosity of 2 pb$^{-1}$ for different extrapolations of the ratio $R_{12} = \sigma(\chi_{c2})/\sigma(\chi_{c1})$

## 7.3 Effect of stricter single leg conditions

In this section, different stricter single leg conditions are applied in the $\chi_c$ simulation to investigate how the number of $\chi_c$ mesons and the kinematic distributions are affected. This is motivated by the ALICE collaboration extending its pp physics programme. One component of this extended programme with high-energy pp collisions at centre-of-mass energies of $\sqrt{s} \approx 13 - 14$ TeV anticipates to select an "offline" analysis with a target integrated luminosity of about 200 pb$^{-1}$. To reduce the stored data size a highly selective software-based event skimming will be performed after data reconstruction [29]. Only certain events will be selected, e.g. the events with a $J/\psi$ fulfilling the selection criteria used in the analysis/simulation above. However, to reduce the data sample for storage further, additional selection criteria might have to be applied.

The different single leg conditions applied are listed in the first column of Tab. 7.3. The other two columns present the expected $p_T$-integrated numbers for a luminosity of 200 pb$^{-1}$ for each of the conditions.

| Single leg condition | $p_T$-integrated $\chi_{c1}$ | $p_T$-integrated $\chi_{c2}$ |
|---|---|---|
| $p_T^e > 1$ GeV/$c$ for both leptons | 423000 | 241000 |
| $p_T^e > 2$ GeV/$c$ for one lepton | 355000 | 182000 |
| $p_T^e > 3$ GeV/$c$ for one leptons | 214000 | 92000 |
| $p_T^e > 2$ GeV/$c$ for both leptons | 127000 | 53000 |

Table 7.3: The first column lists the different single leg conditions applied in the extended simulation of the reconstructed $\chi_c$; if the condition only applies to one lepton, $p_T^e > 1$ GeV/$c$ applies to the other; columns 2 and 3 present the expected $p_T$-integrated numbers at a luminosity of 200 pb$^{-1}$ for the different single leg conditions

The results are definitive:
As seen in Tab. 7.3, the $p_T$-integrated number of $\chi_c$ mesons clearly decreases as the $p_T$-threshold of the single leg cuts increases.
At large momenta the conditions no longer matter, the $p_T$-distributions all converge at higher momenta and there are no more kinematic losses.
Furthermore, the conditions have severe consequences on the minimum $p_T$-reach, see Fig. 7.5. The first single leg cut of $p_T^e > 1$ GeV/$c$ enables measurements down to zero. The greater the $p_T$-threshold, however, the larger the minimum measurable $p_T$. Small momenta are not detectable anymore. Thus, these cuts are advised against.

All distributions must lie below the first least restricted distribution (black), since they are more restricted and more counts are not possible. In other words, all distributions are subsamples of the most generous single leg cut of $p_T^e > 1$ GeV/$c$ (black), this $p_T$-threshold includes all other combinations. However, there are slight fluctuations at $p_T \approx 7$ GeV/$c$, where the red line surpasses the black line, which isn't physically possible. A possible explanation for this is that the final selection criterion applying the photon reconstruction efficiency and conversion probability discussed in Section 5.4 drastically reduces the number of $\chi_c$ mesons by a factor greater than 50, making

statistical fluctuations possible.

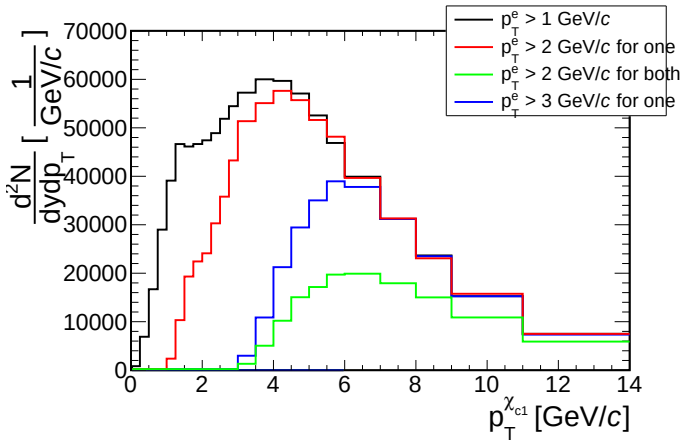


(a) on $\chi_{c1}$

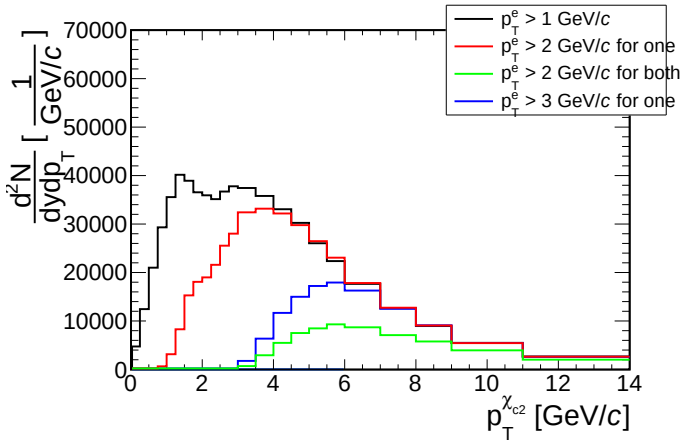


(b) on $\chi_{c2}$

Figure 7.5: Effects of different single leg selection criteria on the estimated numbers of $\chi_{c1}$ and $\chi_{c2}$ mesons. The cuts must all lie within the most generous cut of $p_T^e > 1$ GeV/$c$, see discussion in body text.

# Chapter 8

# Extended Analysis: Single electron momentum smearing

So far, the simulation does not include particle transport through the detector nor the momentum reconstruction. Thus, the bremsstrahlung is not taken into account either. This leads to such narrow distributions as shown in Fig. 4.5, unrealistic to be obtained in an analysis of experimental data.
This section examines the effect of a realistic lepton transverse momentum smearing.

The momentum smearing and bremsstrahlung approach used here is from Yvonne Pachmayer. The effects of the momentum resolution are studied with a full MC simulation from $J/\psi$ to $e^+e^-$ and include the interactions and the momentum reconstruction of $e^+$ and $e^-$.

In a full MC simulation, the invariant mass distribution results from a full simulation of the $J/\psi$ decaying to $e^+e^-$, where the $e^+$ and $e^-$ are reconstructed according to experimental data: the $e^+$ and $e^-$ propagate through the detector, interact with the detector material and are deflected in the magnetic field. As a consequence of electrons and positrons interacting with the material of detectors in energy loss, the lepton kinematic distributions ($p_T$, $\eta$, $\phi$, ...) are reconstructed with the hit information in the TPC. Finally, the invariant mass for the true $J/\psi$ is reconstructed from these reconstructed $e^+e^-$ [25].

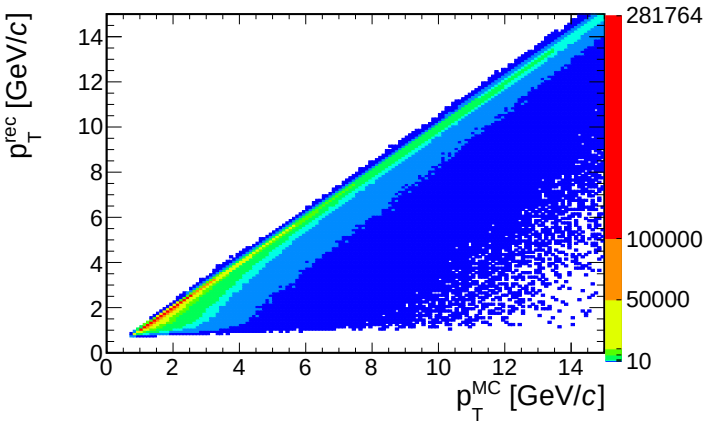


Figure 8.1: Correlation between the true $p_T^{MC}$ and the reconstructed $p_T^{rec}$ of the leptons

The 2-dimensional plot in Fig. 8.1 shows the true MC lepton transverse momentum of the simulation on the x-axis and the reconstructed lepton momentum as described above on the y-axis.
The plot shows a width of approximately 2% around the linear correlation axis, which corresponds to a momentum resolution of $\sim$ 2%. The entries in the lower part of the graph are due to bremsstrahlung. The bremsstrahlung causes a resolution larger than 2%.

The goal of the model is to reconstruct the invariant mass from smeared leptons so that they correspond to the expectations of the full MC simulation. The red entries in Fig. 8.2a show the full MC simulation, the blue entries show the created model of the smeared $p_T$.
This created model randomly generates 70% of the leptons within the limits of a resolution of 2% and the remaining 30% are chosen randomly within the resolution range larger than 2%. Furthermore, the simulated $p_T^{MC}$ value is chosen if the smeared momentum $p_T^{rec} > p_T^{MC}$. After randomly generating these smeared lepton momenta, the four-vectors of the $J/\psi$ mesons are calculated, from which the invariant masses of $J/\psi$ and $\chi_c$ mesons are obtained.
This created model smearing the electrons and positrons works very well, corresponding to the expectations of the full MC simulation.

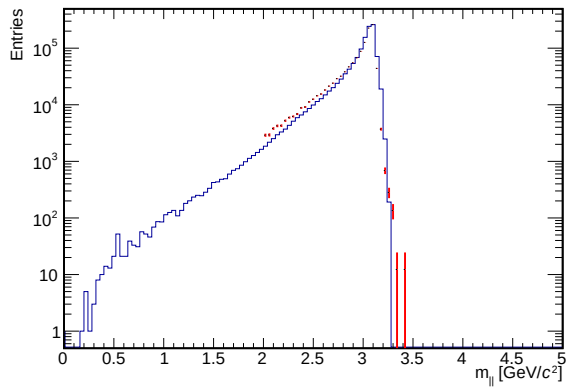


(a) Comparison of smeared model (blue) with the full MC simulation (red)

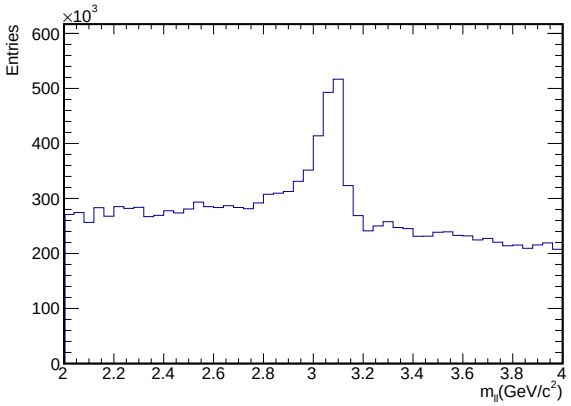


(b) Reconstructed invariant $J/\psi$ mass with combinatorial background in the measurement of electrons and positrons, see discussion in body text

Figure 8.2: Invariant $J/\psi$ mass reconstructed from leptons with smeared momentum

Figure 8.2b shows the invariant mass peak of the $J/\psi$ with background from analysis with real experimental data. The background is caused in the measurement of electrons and positrons. Unlike the MC simulation used in this thesis, the electrons and positrons are not necessarily from $J/\psi$ decays but can have other sources such as $\pi_0$ decays, photon conversions, semileptonic decays of heavy-flavour hadrons etc. The real electron of the $J/\psi$ paired with an electron from the background sources results in the combinatorial background seen in Fig. 8.2b. This background is parametrised by a

second degree polynomial which fits well with experimental data obtained by Yvonne Pachmayer [25]. The $J/\psi$ peak is well distinguishable and the bremsstrahlung devolves into the background signal.
The signal-to-background ratio varies for experimental data, improving with increasing momentum. It is aimed to be around $\sim 0.45$, which is realistic for small momenta, it corresponds to a realistic scenario for $p_T \approx 3 - 4$ GeV/$c$.
From this realistic momentum distribution and realistic background the $\chi_c$ can be calculated.
No background is assumed for the photon.

The combined invariant mass distributions for all three $\chi_c$ mesons resulting from the single electron momentum smearing is shown in Fig. 8.3. The top Fig. 8.3a shows the distribution without combinatorial background, which is then included in the bottom Fig. 8.3b. Both results include all three $\chi_{c0}$, $\chi_{c1}$ and $\chi_{c2}$ invariant mass distributions. However, none of the peaks are properly distinguishable, making signal extraction very difficult.

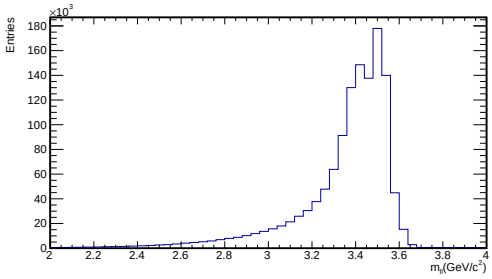


(a) Without combinatorial background

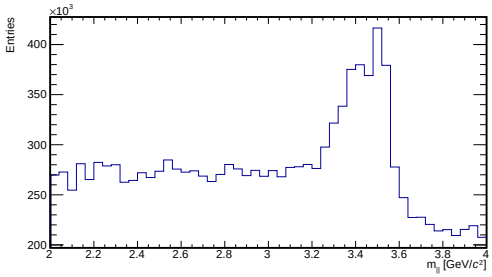


(b) With combinatorial background

Figure 8.3: The reconstructed masses from smeared leptons of all three $\chi_c$ mesons with and without combinatorial background; the three $\chi_c$ mesons are simulated with the same frequency

To improve the signal extraction, the mass difference $\Delta m$ between the reconstructed $\chi_c$ and $J/\psi$ masses is calculated, including only the resolution of the photon. The 2% photon momentum smearing is added.
The peaks can now be measured and fitted in the $\Delta m = m_{\chi_c} - m_{J/\psi}$ spectrum (Fig. 8.4) rather than in the invariant $\chi_c$ mass spectrum (Fig. 8.3). So, the difference rather than the direct reconstructed invariant masses should be considered since only the resolution of the photon goes into this.

To summarise, the effect of lepton smearing results in a randomly distributed momentum resolution, corresponding very well to distributions of the invariant mass of $J/\psi$ from the full simulation. The effect on the invariant $\chi_c$ masses is also clearly visible. The combinatorial background with a signal-to-background ratio of 0.459 is realistic. Figure 8.4 shows that the three $\chi_c$ mesons can indeed be measured experimentally, but only after subtracting the reconstructed invariant mass of the $J/\psi$. These three reconstructed invariant $\chi_{c0}$, $\chi_{c1}$ and $\chi_{c2}$ mass peaks can be fitted with Gaussian (as seen in Fig. 8.4) or Breit Wigner functions (in Fig. A.8 in the Appendix).

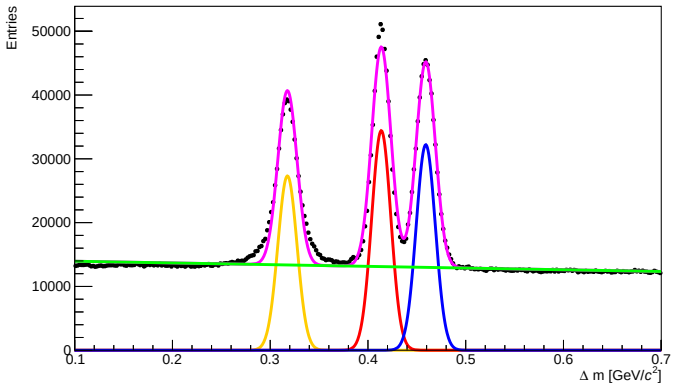


Figure 8.4: The three invariant mass peaks for $\chi_{c0}$, $\chi_{c1}$ and $\chi_{c2}$ subtracted by the invariant mass of $J/\psi$; all invariant masses are reconstructed from smeared leptons so that they correspond to the expectations of the full MC simulation and fitted with Gaussians; the background is fitted with a 2nd degree polynomial; the abundancies are not to scale

# Chapter 9

# Summary and Outlook

This thesis gives estimates for the number of $\chi_{c1}$ and $\chi_{c2}$ mesons expected in pp collisions at the centre-of-mass energy of $\sqrt{s}$ = 13 TeV for ALICE in Run 3 for different luminosities. For this, the $\chi_c$ mesons are simulated and reconstructed in the radiative $J/\psi$ decay channel $\chi_c \rightarrow J/\psi + \gamma$, since the $J/\psi$ has been subject to several studies. The $J/\psi$ is reconstructed in the $e^+e^-$ and the radiative decay channel.

The simulation of the $\chi_c$ mesons is based on measurements of inclusive $J/\psi$ production in pp collisions at $\sqrt{s}$ = 13 TeV and midrapidity by ALICE. Experimental measurements from the LHCb collaboration of the cross section ratios of $\chi_c$ to $J/\psi$ and $\chi_{c2}$ to $\chi_{c1}$ are used to obtain realistic $\chi_c$ kinematics from the $J/\psi$ measurements. These ratios were measured in pp collisions at $\sqrt{s}$ = 7 TeV and forward rapidity. Their minimum transverse-momentum intervals start at 2 GeV/$c$ and 3 GeV/$c$ respectively and the parameterisations from the data are extrapolated to zero for this analysis. The $p_T$-distribution of the $J/\psi$ shows a strong energy dependence. Taking the $\chi_c$ mesons to have a similar energy dependence, the ratios are almost energy independent and can thus be used for realistic estimations.
This $\chi_c$ analysis applies the same selection criteria as a standard realistic $J/\psi$ data analysis. Namely, the rapidity of the mother $\chi_c$ particles and the $p_T$ and rapidity of the leptons are restricted and the $J/\psi$ reconstruction efficiency is applied. This $J/\psi$ reconstruction efficiency is from an analysis of p-Pb collisions at $\sqrt{s_{NN}}$ = 8.16 TeV taken in LHC Run 2 and includes the track reconstruction and electron identification of both leptons. Additionally, the photons from the radiative decay of the $\chi_c$ mesons are restricted with the reconstruction efficiency and conversion probability from the photon analysis in PbPb collisions at $\sqrt{s_{NN}}$ = 5.02 TeV estimated in LHC Run 2, where the photons are converted to $e^+e^-$ in the detector. Especially this last condition on the photons severely decreases the final number of $\chi_c$ mesons. The overall efficiencies after applying all criteria in the simulation are approximately 0.2% for both $\chi_{c1}$ and $\chi_{c2}$.

Additionally, simulations with stricter selection criteria on the single leg leptons of the $J/\psi$ are examined because the data sample for storage in the "offline" analysis is limited and might have to be reduced. Specifically, the minimum $p_T$-thresholds of the

leptons are restricted. The number of $p_T$-integrated $\chi_c$ mesons decreases as the single leg cuts get stricter, i.e. as the $p_T$-threshold of the single leg cuts increases. Further, the conditions have severe consequences on the minimum $p_T$-reach of the $\chi_c$ mesons. The first single leg cut of $p_T^e > 1$ GeV/$c$ enables measurements down to zero, but as this $p_T$-threshold increases, the minimum measurable $p_T$ of the $\chi_c$ mesons increase as well and small momenta are not detectable anymore. Due to these increased $p_T^{\chi_c}$-thresholds the cuts are advised against.
Lastly, the effect of a realistic transverse lepton momentum smearing as in a full MC simulation from $J/\psi$ to $e^+e^-$ and the momentum reconstruction of $e^+$ and $e^-$ is examined, since the simulation does not include particle transport through the detector nor the momentum reconstruction which leads to unrealistic distributions compared to experimental data. The invariant masses of the $\chi_c$ mesons reconstructed in a way that the three $\chi_c$ mesons can indeed be measured experimentally. For this, however, the reconstructed invariant masses of the $\chi_c$ mesons from the smeared leptons cannot be used. The Gaussian and Breit Wigner functions can only be fitted to the mass difference $\Delta m = m_{\chi_c} - m_{J/\psi}$ of the reconstructed invariant $J/\psi$ mass subtracted from the the reconstructed invariant masses of the $\chi_c$ mesons, since only the resolution of the photon goes into this.

The resulting $p_T$-integrated estimated numbers in this simulation are 4260 $\chi_{c1}$ mesons and 2430 $\chi_{c2}$ mesons at 2 pb$^{-1}$, which is the originally foreseen integrated luminosity of pp collisions in LHC Run 3 for ALICE. An ALICE dedicated pp physics programme recording interesting physics probes has a targeted integrated luminosity of 200 pb$^{-1}$. The estimated number of $\chi_c$ mesons is linearly proportional to the integrated luminosity, resulting in 100 times as many $\chi_c$ mesons in this so-called "offline" analysis.
The estimated systematic uncertainties of roughly 5% and 11% for $\chi_{c1}$ and $\chi_{c2}$ respectively are calculated by up- and downward shifts of 10% of the fitted second degree polynomial ratio of $\sigma(\chi_{c2})/\sigma(\chi_{c1})$. This 10%-value is obtained from the uncertainties of the $p_T$-integrated cross section and all other uncertainties are neglected. This shall estimate the effect of different possible extrapolations, since no existing measurements go down to zero $p_T$ which is what this thesis aims to do.

In summary, the results of the estimated numbers of $\chi_c$ mesons are large enough to motivate a search in experimental data for integrated luminosities starting at the low pb$^{-1}$-scale.
The reconstruction model using momentum smearing works well and is satisfactory in that the mesons can indeed be identified from the mass difference of the invariant $\chi_c$ masses and $J/\psi$ mass, both reconstructed from the smeared lepton momenta.

This thesis shows several limitations.
Firstly, the experimentally measured data used as input for the simulation are measured under conditions different to those considered. For instance, the ratios of the cross section ratios of $\chi_c$ to $J/\psi$ and $\chi_{c2}$ to $\chi_{c1}$ used are measured at different centre-of-mass energies and rapidity ranges. All experimental data is from Run 2, so that effects of some changes in the hardware and reconstruction algorithm from Run 2 to Run 3 can only be predicted. For example, the lepton and photon efficiencies and particle detec-

tion will be slightly different due to the upgraded detector in Run 3. The estimations in this thesis assume them to be the same. Additionally, the simulations are based on $J/\psi$ measurements at a centre of mass energy of $\sqrt{s}$ = 13 TeV. The LHC decided to preform Run 3 at $\sqrt{s}$ = 13.6 TeV rather than $\sqrt{s}$ = 13 TeV only this July, so new simulations have to be generated. The cross section will increase slightly with this increased centre-of-mass energy.
Both used experimentally measured ratios do not go down to zero $p_T$. Another substantial limitation of this thesis is that only the ratio of $\sigma(\chi_{c2})/\sigma(\chi_{c1})$ was extrapolated to examine potential scenarios at $p_T$-values below the measured 2 GeV/$c$. This could be improved on the one hand by choosing different types of extreme extrapolations (linear, constant, exponential,...) and not just shifting the measured second degree polynomial ratio. On the other hand, theoretical calculations could be used for better predictions at low momenta.
Finally, the uncertainty estimation in this thesis does not consider all sources. The estimated systematic uncertainty is merely calculated from the effect of the shift of the fitted polynomial $\sigma(\chi_{c2})/\sigma(\chi_{c1})$ ratio as discussed before. The same could have been done for the used $\sigma(\chi_c)/\sigma(J/\psi)$ ratio. Also, relevant measurements from other collaborations could have been implemented to see how other experimental data changes the predictions.

Overall, even with all suggestions to improve the estimations, the results should be within the same order of magnitude and points to promising $\chi_c$ measurements in ALICE in Run 3 within the foreseen pp physics programme.

# Appendix A

# Appendix

## A.1 ITS2

| | ITS | ITS2 |
|---|---|---|
| Technology | Hybrid pixel, drift, strip | MAPS |
| Max rate (Pb-Pb) | 1 kHz | 100 kHz |
| Thickness per layer | ~ 1.14% $X_0$ | Inner barrel: 0.3% $X_0$, Outer barrel: 1% $X_0$ |
| Pixel size | 425 µm x 50 µm | 27 µm x 29 µm |
| Spatial res. (rΦ x z) | 12 µm x 100 µm | 5 µm x 5 µm |
| Radius | 39 - 430 mm | 22 – 395 mm |
| Rapidity range | $\|\eta\| < 0.9$ | $\|\eta\| < 1.3$ |
| Layers | 6 | 7 |
| Readout | Analog (drift, strip), Digital (pixel) | Digital |

Figure A.1: Comparison of the ITS detector in Run 1 and 2 (ITS) and Run 3 (ITS2)

## A.2 $\chi_c$ properties

| name | PythiaId | mass/GeV | width/GeV | max$_D m/GeV$ | 3*charge | 2*spin | lifetime*c/mm |
|---|---|---|---|---|---|---|---|
| $\chi_{c0}$ | 10441 | 3.4147500e+00 | 1.0500000e-02 | 5.0000000e-02 | 0 | 0 | 0.0000000e+00 |
| $\chi_{c1}$ | 20443 | 3.5106600e+00 | 8.4000000e-04 | 1.0000000e-02 | 0 | 2 | 0.0000000e+00 |
| $\chi_{c2}$ | 445 | 3.5562000e+00 | 1.9300000e-03 | 6.0000000e-03 | 0 | 4 | 0.0000000e+00 |

Table A.1: $\chi_c$ properties from evt.pdl; Updated by R. Godang. The format and convention are based on the current evt.pdl and PDG 2012; from 5/10/2013

## A.3 Decay table

```
#####
Decay chi_c0
1.0 gamma   J/psi                                   SVP; #[Reconstructed PDG2011]
Enddecay

Decay chi_c1
1.0 gamma   J/psi                                   VVP 1.0 0.0 0.0 0.0 0.0 0.0 0.0 0.0;
Enddecay

Decay chi_c2
1.0 gamma   J/psi                                   TVP; #[Reconstructed PDG2011]
Enddecay

Decay J/psi
1.000 e+   e-               PHOTOS VLL;
Enddecay

End
```

Figure A.2: A documentation of the simulated decays in the decay table CHICTOJPSITOELE.DEC [19]. SVP describes a radiative decays of a scalar to a vector particle; VVP: vector to vector particle; TVP: tensor to vetor particle [30]

## A.4 Additional kinematic distributions

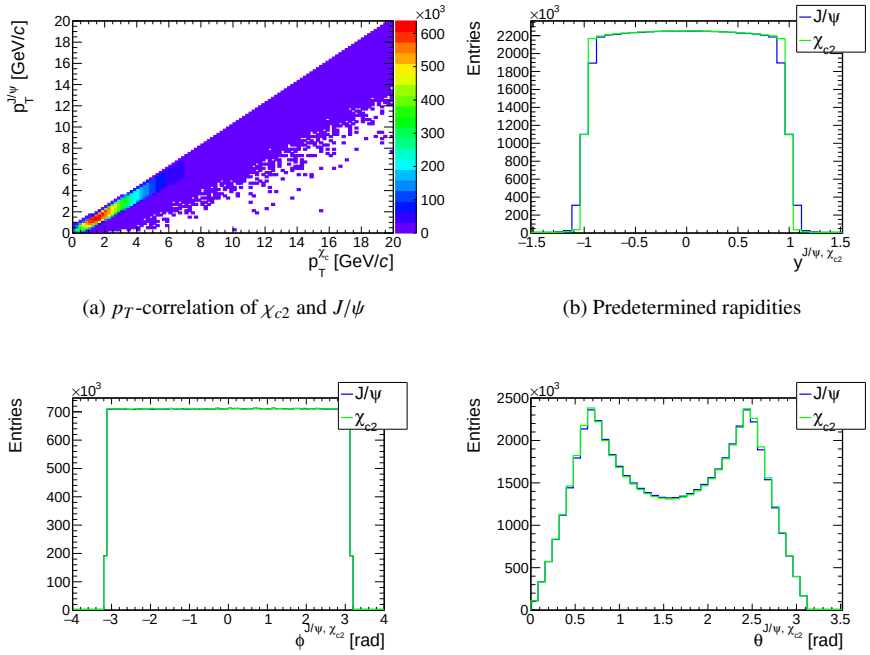


(a) $p_T$-correlation of $\chi_{c2}$ and $J/\psi$

(b) Predetermined rapidities

(c) Distribution of angle $\phi$ in $xy$-plane

(d) Distribution of angle $\theta$ along beam axis

Figure A.3: Kinematic distributions for $\chi_{c2}$ and the corresponding $J/\psi$

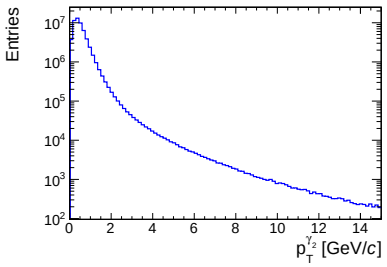


(a) $p_T$-distribution of photon

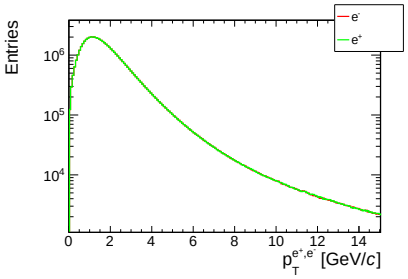


(b) $p_T$-distribution of lepton and antilepton

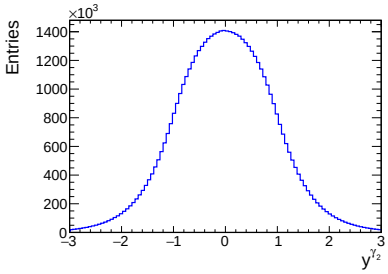


(c) rapidity $y^{\gamma}$ of photon

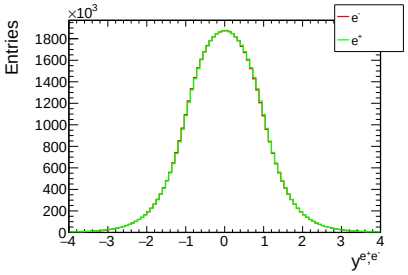


(d) rapidity $y^{e}$ of lepton and antilepton

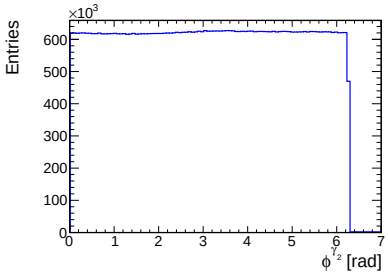


(e) $\phi$-distribution of photon

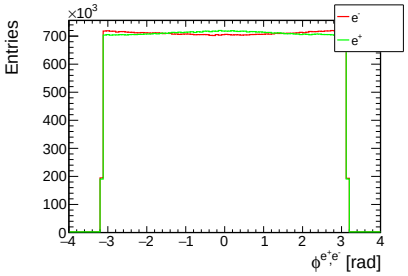


(f) $\phi$-distribution of lepton and antilepton

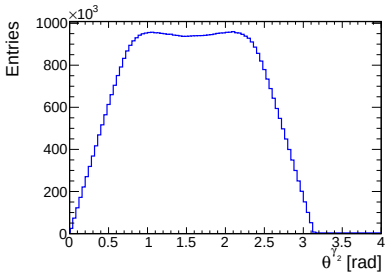


(g) $\theta$-distribution of photon

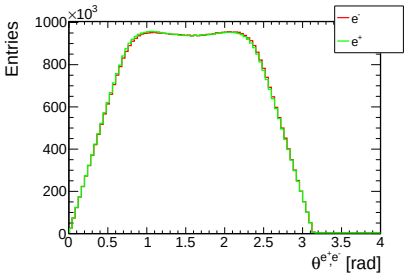


(h) $\theta$-distribution of lepton and antilepton

Figure A.4: Kinematics of photon from the $\chi_{c2}$ decay and lepton and antilepton $e^+$ and $e^-$ from the $J/\psi$ from the $\chi_{c2}$ decay

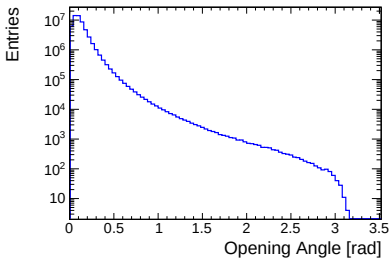


(a) Opening angle of $J/\psi$ and $\chi_{c2}$

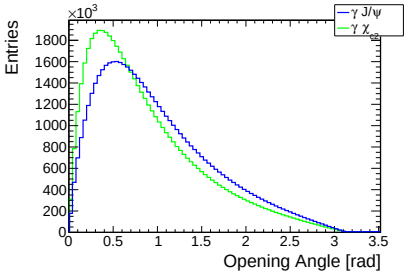


(b) Opening angle of photon and $J/\psi$ as well as photon and $\chi_{c2}$

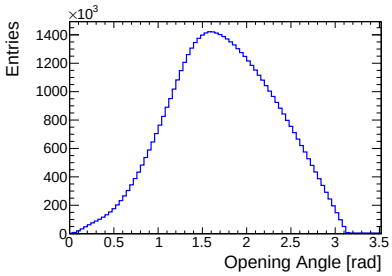


(c) Opening Angle of lepton and antilepton

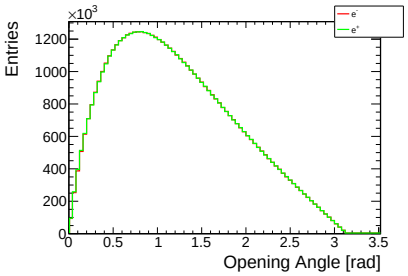


(d) Opening Angle of photon and lepton as well as photon and antilepton

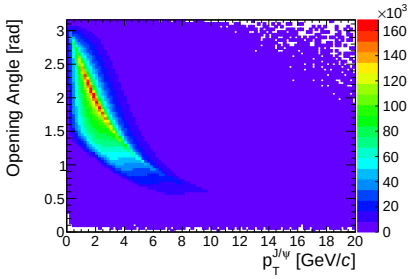


(e) Correlation of the opening Angle of lepton and antilepton and the transverse momentum of $J/\psi$ $p_T^{J/\psi}$

Figure A.5: Different opening angles for $\chi_{c2}$ and the corresponding $J/\psi$, $e^+e^-$ and photon

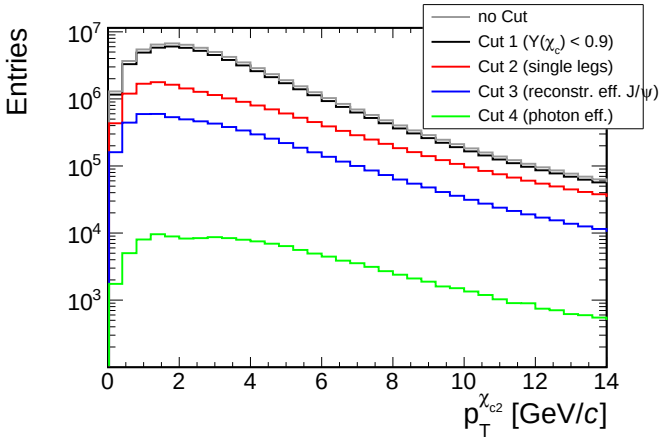


Figure A.6: Effects of applied selection criteria on $\chi_{c2}$

## A.5 Effect of selection criteria

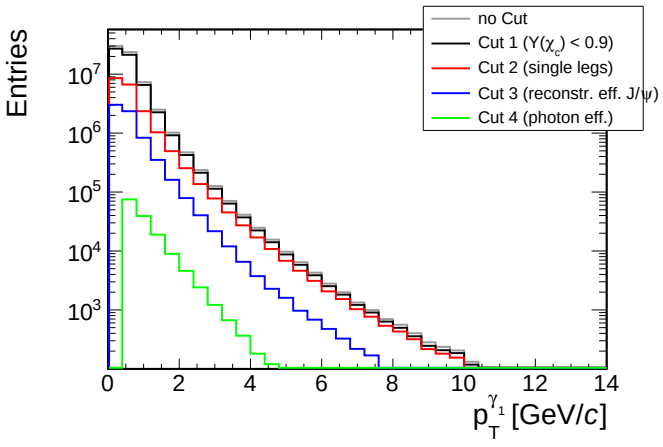


(a) $\chi_{c1}$-photon, denoted as $\gamma_1$

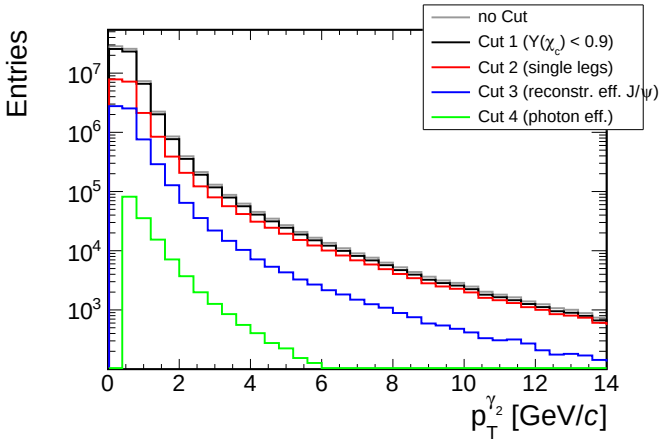


(b) $\chi_{c2}$-photon, denoted as $\gamma_2$

Figure A.7: Effect of selection criteria on the $p_T$-distribution of the photons of the $\chi_{c1}$ and $\chi_{c2}$ mesons

## A.6 Single leg momentum smearing fitted with Breit Wigner

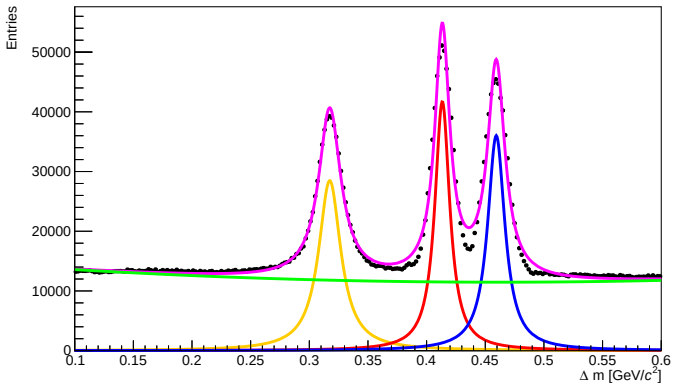


Figure A.8: The three invariant mass peaks for $\chi_{c0}$, $\chi_{c1}$ and $\chi_{c2}$ subtracted by the invariant mass of $J/\psi$; all invariant masses are reconstructed from smeared leptons so that they correspond to the expectations of the full MC simulation and fitted with Breit Wigner functions; the abundancies are not to scale

# Bibliography


[1] M. Thomson, *Modern Particle Physics*. Cambridge University Press, 2013.

[2] C. Burgard and D. Galbraith, "A standard diagram of the current standard model of physics.". https://texample.net/tikz/examples/model-physics/.

[3] S. Borsanyi, "Frontiers of finite temperature lattice QCD," *EPJ Web Conf.* **137** (2017) 01006, arXiv:1612.06755 [hep-lat].

[4] P. Braun-Munzinger and J. Stachel, "The quest for the quark–gluon plasma," *Nature* **448** (Jul, 2007) . https://doi.org/10.1038/nature060801.

[5] **ALICE** Collaboration, "Inclusive J/$\psi$ production at midrapidity in pp collisions at $\sqrt{s}$ = 13 TeV," *The European Physical Journal C* **81** no. 12, (Dec, 2021) . https://doi.org/10.1140%2Fepjc%2Fs10052-021-09873-4.

[6] **ALICE** Collaboration, S. Acharya *et al.*, "Inclusive J/$\psi$ production at midrapidity in pp collisions at $\sqrt{s}$ = 13 TeV," *Eur. Phys. J. C* **81** no. 12, (2021) 1121, arXiv:2108.01906 [nucl-ex].

[7] **Particle Data Group** Collaboration, R. L. Workman and Others, "Review of Particle Physics," *PTEP* **2022** (2022) 083C01.

[8] **CDF** Collaboration, "Production of $J/\psi$ mesons from $\chi_c$ Meson Decays in pp Collisions at $\sqrt{s}$ = 1.8 TeV," *Physical Review Letters* **79** no. 4, (1997) 578–583. https://journals.aps.org/prl/pdf/10.1103/PhysRevLett.79.578.

[9] **LHCb** Collaboration, "Measurement of the ratio of prompt $\chi_c$ to J/$\psi$ production in pp collisions at $\sqrt{s}$ = 7 tev," *Physics Letters B* **718** no. 2, (2012) 431–440. https://www.sciencedirect.com/science/article/pii/S0370269312011343.

[10] **CDF** Collaboration, "Measurement of $\sigma_{\chi_{c2}}\mathcal{B}(\chi_{c2} \to \mathrm{J}/\psi\gamma)/\sigma_{\chi_{c1}}\mathcal{B}(\chi_{c1} \to \mathrm{J}/\psi\gamma)$ in $p\overline{p}$ collisions at $\sqrt{s}$ = 1.96 TeV," *Physical Review Letters* **98** no. 23, (Jun, 2007) . https://doi.org/10.1103%2Fphysrevlett.98.232001.

[11] **LHCb** Collaboration, "Measurement of the cross-section ratio $\sigma(\chi_{c2})/\sigma(\chi_{c1})$ for prompt $\chi_c$ production at $\sqrt{s}$ = 7 TeV," *Physics Letters B* **2013** no. 10, (Oct, 2013) . https://arxiv.org/abs/1307.4285.

[12] **LHCb** Collaboration, "Measurement of the cross-section ratio $\sigma(\chi_{c2})/\sigma(\chi_{c1})$ for prompt $\chi_c$ production at $\sqrt{s}$ = 7 tev," *Physics Letters B* **714** no. 2-5, (Aug, 2012) 215–223. https://doi.org/10.1016%2Fj.physletb.2012.06.077.

[13] **CMS** Collaboration, "Measurement of the relative prompt production rate of $\chi_{c2}$ and $\chi_{c2}$ in pp collisions at $\sqrt{s}$ = 7 TeV," *The European Physical Journal C* **72** no. 12, (Dec, 2012) . https://doi.org/10.1140%2Fepjc%2Fs10052-012-2251-3.

[14] **LHCb** Collaboration, "Measurement of the prompt-production cross-section ratio $\sigma(\chi_{c2})/\sigma(\chi_{c1})$ in $p$pb collisions at $\sqrt{s_{NN}}$ = 8.16 TeV," *Physical Review C* **103** no. 6, (Jun, 2021) . https://doi.org/10.1103%2Fphysrevc.103.064905.

[15] **HERA-B** Collaboration, "Production of the charmonium states $\chi_{c1}$ and $\chi_{c2}$ in proton nucleus interactions at $\sqrt{s}$ = 41.6 gev" *Physical Review D* **79** no. 1, (Jan, 2009) . https://doi.org/10.1103%2Fphysrevd.79.012001.

[16] **ALICE** Collaboration, K. Aamodt *et al.*, "The ALICE experiment at the CERN LHC," *JINST* **3** (2008) S08002.

[17] J. Alme *et al.*, "The ALICE TPC, a large 3-dimensional tracking device with fast readout for ultra-high multiplicity events," *Nucl. Instrum. Meth. A* **622** (2010) 316–367, arXiv:1001.1950 [physics.ins-det].

[18] **ALICE** Collaboration, B. Abelev *et al.*, "Upgrade of the ALICE Experiment: Letter Of Intent," *J. Phys. G* **41** (2014) 087001.

[19] ALICEO2Group, "ALICE O2 Analysis Framework.". https://aliceo2group.github.io/analysis-framework/docs/.

[20] D. J. Lange, "The EvtGen particle decay simulation package," *Nucl. Instrum. Meth. A* **462** (2001) 152–155.

[21] "PHOTOS - a universal Monte Carlo for QED radiative corrections: version 2.0" *Computer Physics Communications* **79** no. 2, (1994) 291–308.

[22] **ALICE** Collaboration, S. Acharya *et al.*, "Energy dependence of forward-rapidity J/$\psi$ and $\psi$ (2S) production in pp collisions at the LHC," *European Physical Journal C* **77** no. 6, (June, 2017) 392, arXiv:1702.00557 [hep-ex].

[23] **LHCb** Collaboration, "Measurement of the ratio of prompt $\chi_c$ to $J/\psi$ production in $pp$ collisions at $\sqrt{s}$ = 7 TeV." HEPData (collection), 2012. https://doi.org/10.17182/hepdata.59360.

[24] **LHCb** Collaboration, "Measurement of the relative rate of prompt $\chi_{c0}$, $\chi_{c1}$ and $\chi_{c2}$ production at $\sqrt{s}$ = 7 TeV." HEPData (collection), 2016. https://doi.org/10.17182/hepdata.66239.

[25] Private Communication with Y. Pachmayer.

[26] Private Communication with Dr. M. Danish.

[27] Private Communication with Dr. A. Marin.

[28] Private Communication with N. Tatsch.

[29] **ALICE** Collaboration, "Future high-energy pp programme with ALICE,". https://cds.cern.ch/record/2724925.

[30] D. J. Lange, "EvtGen Documentation.". https://evtgen.hepforge.org/doc/models.html.

# Acknowledgements

In particular I would like to thank my supervisor Priv. Doz. Dr. Yvonne Pachmayer for her effort and everything she taught me as well as her patience and answering my many questions.

I would also like to thank Prof. Dr. Johanna Stachel for being my second examiner.

To Dr. Jana Crkovská and Fabi Linsenmeier, thank you very much for proofreading.

# Erklärung

Ich versichere, dass ich diese Arbeit selbstständig verfasst und keine anderen als die angegebenen Quellen und Hilfsmittel benutzt habe.

Heidelberg, den 22.08.2022,